



HAL
open science

METAL: The Metal Evolution, Transport, and Abundance in the Large Magellanic Cloud Hubble Program. III. Interstellar Depletions, Dust-to-Metal, and Dust-to-Gas Ratios versus Metallicity

Julia Roman-Duval, Edward Jenkins, Kirill Tchernyshyov, Christopher Clark, Annalisa de Cia, Karl Gordon, Aleksandra Hamanowicz, Vianney Lebouteiller, Marc Rafelski, Karin Sandstrom, et al.

► **To cite this version:**

Julia Roman-Duval, Edward Jenkins, Kirill Tchernyshyov, Christopher Clark, Annalisa de Cia, et al.. METAL: The Metal Evolution, Transport, and Abundance in the Large Magellanic Cloud Hubble Program. III. Interstellar Depletions, Dust-to-Metal, and Dust-to-Gas Ratios versus Metallicity. The Astrophysical Journal, 2022, 928 (1), pp.90. 10.3847/1538-4357/ac5248 . hal-03695706

HAL Id: hal-03695706

<https://hal.science/hal-03695706>

Submitted on 16 Jun 2022

HAL is a multi-disciplinary open access archive for the deposit and dissemination of scientific research documents, whether they are published or not. The documents may come from teaching and research institutions in France or abroad, or from public or private research centers.

L'archive ouverte pluridisciplinaire **HAL**, est destinée au dépôt et à la diffusion de documents scientifiques de niveau recherche, publiés ou non, émanant des établissements d'enseignement et de recherche français ou étrangers, des laboratoires publics ou privés.



Distributed under a Creative Commons Attribution 4.0 International License



METAL: The Metal Evolution, Transport, and Abundance in the Large Magellanic Cloud Hubble Program. III. Interstellar Depletions, Dust-to-Metal, and Dust-to-Gas Ratios versus Metallicity

Julia Roman-Duval¹, Edward B. Jenkins², Kirill Tchernyshyov³, Christopher J. R. Clark¹, Annalisa De Cia⁴, Karl D. Gordon¹, Aleksandra Hamanowicz¹, Vianney Lebouteiller⁵, Marc Rafelski¹, Karin Sandstrom⁶, Jessica Werk³, and Petia Yanchulova Merica-Jones¹

¹ Space Telescope Science Institute, 3700 San Martin Drive, Baltimore, MD 21218, USA

² Department of Astrophysical Sciences, Peyton Hall, Princeton University, Princeton, NJ 08544-1001 USA

³ Department of Astronomy Box 351580, University of Washington, Seattle, WA 98195, USA

⁴ Department of Astronomy, University of Geneva, Chemin Pegasi 51 1290 Versoix, Switzerland

⁵ AIM, CEA, CNRS, University Paris-Saclay, University Paris Diderot, Sorbonne, Paris City F-91191 Gif-sur-Yvette, France

⁶ Center for Astrophysics and Space Sciences, Department of Physics, University of California, 9500 Gilman Drive La Jolla, San Diego, CA 92093, USA

Received 2021 August 5; revised 2021 December 17; accepted 2022 February 4; published 2022 March 29

Abstract

The metallicity and gas density dependence of interstellar depletions, the dust-to-gas (D/G), and dust-to-metal (D/M) ratios have important implications for how accurately we can trace the chemical enrichment of the universe, either by using FIR dust emission as a tracer of the ISM or by using spectroscopy of damped Ly α systems to measure chemical abundances over a wide range of redshifts. We collect and compare large samples of depletion measurements in the Milky Way (MW), Large Magellanic Cloud (LMC) ($Z = 0.5 Z_{\odot}$), and Small Magellanic Cloud (SMC) ($Z = 0.2 Z_{\odot}$). The relations between the depletions of different elements do not strongly vary between the three galaxies, implying that abundance ratios should trace depletions accurately down to 20% solar metallicity. From the depletions, we derive D/G and D/M. The D/G increases with density, consistent with the more efficient accretion of gas-phase metals onto dust grains in the denser ISM. For $\log N(\text{H}) > 21 \text{ cm}^{-2}$, the depletion of metallicity tracers (S, Zn) exceeds -0.5 dex, even at 20% solar metallicity. The gas fraction of metals increases from the MW to the LMC (factor 3) and SMC (factor 6), compensating for the reduction in total heavy element abundances and resulting in those three galaxies having the same neutral gas-phase metallicities. The D/G derived from depletions are respective factors of 2 (LMC) and 5 (SMC) higher than the D/G derived from FIR, 21 cm, and CO emission, likely due to the combined uncertainties on the dust FIR opacity and on the depletion of carbon and oxygen.

Unified Astronomy Thesaurus concepts: [Interstellar medium \(847\)](#); [Interstellar dust processes \(838\)](#); [Galaxy chemical evolution \(580\)](#); [Gas-to-dust ratio \(638\)](#); [Interstellar abundances \(832\)](#)

1. Introduction

Over a galaxy's lifetime, metals are produced in stars and deposited into the interstellar medium (ISM). These metals cycle between different phases of the ISM: some remain in the gas at different temperatures and pressures, others are locked into dust, and others are ejected through galactic winds into the circumgalactic medium, where they can rain back down into the ISM (Oppenheimer & Davé 2008). This incessant cycle of material between stars, interstellar gas and dust, and galaxy halos drives galaxy evolution. A critical, yet poorly understood, aspect of this baryon cycle is the depletion of metals from the gas to the dust phase via dust formation, and vice versa, the return of heavy elements from the dust to the gas phase via dust destruction. The parameters describing the life cycle of metals in the neutral ISM are the dust-to-metal mass ratio (D/M, the mass fraction of metals locked up in dust grains) and the dust-to-gas mass ratio ($D/G = D/M \times Z$, where Z is the metallicity).

D/M and D/G are theoretically expected to vary with metallicity (e.g., Asano et al. 2013; Feldmann 2015; Zhukovska et al. 2016; Mattsson 2020). Above a critical

metallicity at which the dust input rate from evolved stars (AGB + supernovae) and ISM dust growth balances the dust destruction by supernova (SN) shockwaves and dilution by inflows of pristine gas, the D/M is predicted to be high with most metals locked in the dust phase. Below this critical metallicity, dust growth in the ISM is not efficient enough to counterbalance destruction and dilution effects. In this case, the D/M is expected to be low and determined by the input of stellar dust sources. Assuming the fiducial parameters in Feldmann (2015), including a molecular depletion time of 2 Gyr (Bigiel et al. 2008) and timescale of dust growth in the ISM at solar metallicity of 500 Myr for volume densities of 100 cm^{-3} (Hirashita 2000; Asano et al. 2013), the critical metallicity separating low and high D/M and D/G is about 10%–15% solar.

D/G and D/M can be measured in nearby galaxies using two distinct approaches and observational techniques. The gas and dust content of nearby galaxies can be estimated using emission-based tracers, specifically FIR emission to trace interstellar dust, and 21 cm and CO rotational emission to trace gas. Their ratio provides D/G, and if the metallicity of the system is known, also D/M. Alternatively, D/M and D/G can be estimated from depletion measurements using UV spectroscopy of interstellar absorption lines. The depletion of element X, $\delta(X)$, is the logarithm of the fraction of X in the gas



Original content from this work may be used under the terms of the [Creative Commons Attribution 4.0 licence](#). Any further distribution of this work must maintain attribution to the author(s) and the title of the work, journal citation and DOI.

phase, and is given by

$$\delta(X) = \log_{10}\left(\frac{N(X)}{N(H)}\right) - \log_{10}\left(\frac{X}{H}\right)_{\text{tot}}, \quad (1)$$

where $(X/H)_{\text{tot}}$ are total ISM abundances, assumed to equate the abundances in the photospheres of young stars recently formed out of the ISM. Knowing depletions, and therefore also the fraction of metals in the dust, for elements that are the main constituents of dust yields D/M and D/G .

Variations in D/M and D/G with metallicity, and how well such variations can be observationally constrained, have important implications for galaxy evolution and how accurately we can track the chemical enrichment of the universe. First, a comprehensive understanding of the variations of D/M and D/G with metallicity is required to estimate gas masses based on far-infrared dust emission in both nearby (Bolatto et al. 2011; Schrubba et al. 2011) and distant (Rowlands et al. 2014) galaxies. Second, understanding depletion patterns is critical to the interpretation of gas-phase abundance measurements in damped Ly α systems (DLAs). DLAs are neutral gas absorption systems with $\log N(H) > 20.3 \text{ cm}^{-2}$ observed over a wide range of redshifts using quasar absorption spectroscopy (e.g., Rafelski et al. 2012; Quiret et al. 2016; De Cia et al. 2018). Thanks to their H I and metallic absorption lines, DLAs trace the chemical enrichment of the universe over cosmic times, and carry the majority of metals at high redshift (Péroux & Howk 2020). However, gas-phase abundance measurements in DLAs have to be corrected for the depletion of metals from the gas to the dust phase, particularly at metallicities $>1\%$ solar, and thus tracking the chemical enrichment of the universe through DLA spectroscopy requires an understanding of how the fraction of metals in the dust phase varies with metallicity. This can be understood in nearby galaxies such as the Milky Way and Magellanic Clouds, where gas-phase, stellar, and ionized gas abundances can be measured.

On the one hand, measurements of D/M and D/G in nearby galaxies as a function of metallicity from observations using FIR, H I 21 cm and CO emission to trace dust, atomic, and molecular gas (e.g., Herrera-Camus et al. 2012; Rémy-Ruyer et al. 2014; De Vis et al. 2019) confirm the theoretical prediction that the D/G sharply decreases at a metallicity of 10%–20% solar (see Figure 9(a) in the review by Galliano et al. (2018), and references therein). The emission-based D/G measurements in nearby galaxies follow the model tracks from Feldmann (2015), with the best agreement obtained for the parameter $\gamma = 3 \times 10^4$, where γ is the ratio of the molecular gas consumption time by star formation to the timescale for dust growth in the ISM. On the other hand, Figure 9 in Galliano et al. (2018) shows that D/G measurements obtained from abundance ratios (in particular $[Zn/Fe]$, see De Cia et al. 2016) in DLAs over a wide range of redshifts follow a different trend, close to linear with metallicity.

This tension between measurements of D/G obtained with emission-based tracers (FIR, 21 cm, CO) in nearby galaxies, rest-frame UV absorption in DLAs, and chemical evolution models could be explained by several factors. First, emission-based tracers suffer from substantial degeneracies and systematics: dust mass estimates are degenerate with the assumed FIR opacity of dust, which has been shown to vary (Stepnik et al. 2003; Köhler et al. 2012; Demyk et al. 2017) and is not well-constrained observationally (Clark et al. 2019). In estimating dust masses from the FIR, there is also a potential

bias (underestimation of the dust mass) due to the integrated nature of the measurement of dust surface densities that can vary on small scales (Galliano et al. 2011). Gas masses estimated from 21 cm and CO emission also suffer from substantial systematics. The molecular gas mass estimates rely on an assumed CO-to-H₂ conversion factor (Bolatto et al. 2013), which is also poorly constrained and degenerate with D/G measurements (Roman-Duval et al. 2014). Another potential issue in estimating atomic gas masses from 21 cm emission is that masses are often estimated from integrated measurements associated with a region that is spatially more extended than the region detected in dust emission (either on the sky or along the line of sight), leading to a possible overestimation of the gas mass. Thus, the systematic uncertainty on D/G estimates based on emission tracers could very well amount to a factor of several, perhaps up to an order of magnitude, and the effects described above would preferentially underestimate the D/G .

Second, the relation between depletions and abundance ratios in DLAs is calibrated on depletion measurements obtained in the Milky Way at solar metallicity (a local calibration is required for at least one element, usually Zn; see De Cia et al. 2016). It is possible that nucleosynthetic effects modify this relation at low metallicity. Indeed, Zn could behave like an α -process element (Ernandes et al. 2018), with the stellar $[Zn/Fe]$ ratio being enhanced in some stellar populations in an age- and metallicity-dependent way (Duffau et al. 2017; da Silveira et al. 2018; Delgado Mena et al. 2019). Based on a small sample in the Large Magellanic Cloud (LMC, 50% solar metallicity; see Russell & Dopita 1992) and the Small Magellanic Cloud (SMC, 20% solar metallicity; see Russell & Dopita 1992), De Cia (2018) show that the calibration of iron depletions, which correlate tightly with the depletions of other elements (Jenkins 2009; Roman-Duval et al. 2021), as a function of $[Zn/Fe]$ does not appear to change significantly between the Milky Way, LMC, and SMC, where interstellar depletions can be estimated from the gas and stellar abundances (Jenkins 2009; Tchernyshyov et al. 2015; De Cia 2018; Roman-Duval et al. 2021), as opposed to inferred from abundance ratios. Nevertheless, only a few depletion measurements were available in the LMC until the METAL (GO-14675) large Hubble Space Telescope (HST) program obtained UV spectra of 32 sight lines in the LMC (Roman-Duval et al. 2019, 2021).

In this paper, we compile recent depletion measurements in the Milky Way, LMC, and SMC, and compare the relations between depletions of different elements and their abundance ratios between these three galaxies. From the depletions, we compute D/G and D/M and examine the relation between depletions, D/M , D/G , and hydrogen column density, which has been shown to be a driver of the D/M and D/G (Roman-Duval et al. 2017; Chiang et al. 2018, 2021; Roman-Duval et al. 2021). Additionally, we examine the metallicity dependence of depletions, D/M , and D/G by also including D/G estimates in nearby galaxies obtained from FIR measurements. The results presented in this paper lay the groundwork for deriving calibrations of depletions as a function of abundance ratios that can be applied to DLAs in order to estimate the metal and dust content of the universe over cosmic times, which will be presented in the upcoming METAL IV paper (J. Roman-Duval et al. 2022, in preparation).

Table 1
Reference Abundances of Young Stars (a Proxy for the ISM Total Abundances) in the MW, LMC, and SMC

Element	W_X	MW $12+\log(X/H)_{\text{tot}}$	Reference ^a	LMC $12+\log(X/H)_{\text{tot}}$	Reference ^a	SMC $12+\log(X/H)_{\text{tot}}$	Reference ^a
C	12.01	8.46	1	7.94	2	7.52	2
O	16.0	8.76	1	8.50	2	8.14	2
Mg	24.3	7.62	1	7.26	2	6.95	6
Si	28.1	7.61	1	7.35	2	6.86	6
S	32.06	7.26	1	7.13	3	6.47	6
Ti	47.87	5.00	1	4.76	4	4.30	6
Cr	52.0	5.72	1	5.37	2	4.99	6
Fe	55.85	7.54	1	7.32	2	6.85	6
Ni	58.7	6.29	1	5.92	2	5.57	6
Cu	63.55	4.34	1	3.79	5
Zn	65.4	4.70	1	4.31	2	3.91	6

Note.

^a (1) Jenkins (2009), who adopt solar abundances from Lodders (2003); (2) Tchernyshyov et al. (2015); (3) $12 + \log(S/H) = [S/Fe] + (S/Fe)_{\odot} + 12 + \log(Fe/H)$ with $[S/Fe]$ from Hill et al. (1995), $12 + \log(Fe/H)$ from (2), and $(S/Fe)_{\odot}$ from Lodders (2021); (4) Welty & Crowther (2010); (5) Asplund et al. (2009) scaled by factor 0.5 (−0.3 dex); (6) Jenkins & Wallerstein (2017), who scale proto-solar abundances from Lodders (2003) by a factor 0.22 (−0.6 dex).

The paper is organized as follows. In Section 2, we present the details of the depletion measurements compiled in this paper. The depletions of different elements are compared in Section 3. The derivation of D/M and D/G is presented in Section 4, and the relation between depletions, D/M, D/G, and hydrogen column density is examined in Section 5. We infer the dust composition from depletions in the Milky Way (MW), LMC, and SMC in Section 6. We examine the metallicity dependence of D/G based on the new depletion measurements in Section 7. Results are summarized in the conclusion (Section 8).

2. Interstellar Depletions from the Literature

In order to perform a comparison of depletions and their environmental variations between the MW, LMC, and SMC, we compile gas-phase abundance and depletion measurements in those galaxies from the literature. Depletions for element X are computed from gas-phase column density measurements, $\log N(X)$, and column density of hydrogen $N(H) = N(H\text{ I}) + 2N(H_2)$ following Equation (1).

Depletions for different elements are observed to tightly correlate with each other, as observed by Jenkins (2009). They introduced the F_* parameter to describe the collective advancement of depletions in the Milky Way, with $F_* = 0$ corresponding to the least depleted sight lines in the MW with $\log N(H) > 19.5 \text{ cm}^{-2}$ (implying negligible ionization corrections) and $F_* = 1$ corresponding to the most depleted velocity component toward ζ Oph. Following Jenkins (2009), the depletion of element X can be modeled from F_* by

$$\delta(X) = A_X(F_* - z_X) + B_X, \quad (2)$$

where the A_X , B_X , and z_X coefficients are obtained from examining and fitting the relation between depletion measurements for different elements toward a sufficiently large sample of sight lines. The term z_X is introduced to remove the covariance between errors on the slope (A_X) and intercept (B_X) of the relation. The F_* parameter is critical in inferring depletions for elements when they cannot be measured, and thus for estimating the dust-to-metal and dust-to-gas ratios in different systems.

In the following sections, we present the compilation of depletion measurements, as well as estimates of A_X , B_X , and z_X , in the MW, LMC, and SMC.

2.1. Milky Way

In the Milky Way, Jenkins (2009, their Table 7) provide a comprehensive compilation of gas-phase abundances and interstellar depletions measured from Copernicus and HST spectra. Of the 276 sight lines and velocity components included in the Jenkins (2009) study (their Table 2), we select the 226 objects with robustly determined H I column densities, and determined H_2 column densities or upper limits on $N(H_2)$ consistent with H_2 fractions, defined as $2N(H_2)/(N(H\text{ I}) + 2N(H_2))$, lower than 10%. For each of those sight lines and velocity components, we only retain gas-phase column density measurements ($\log N(X)$) and discard upper or lower limits on $\log N(X)$, where X is one of the 17 elements included in the Jenkins (2009) study (C, N, O, Mg, Si, P, S, Cl, Cr, Mn, Fe, Ni, Cu, Zn, Ge, Kr, and Ti). We note that the remaining determinations sample the parameter space as well as the full sample (including limits). Additionally, we only include sight lines with $\log N(H) > 19.5 \text{ cm}^{-2}$, because sight lines with lower hydrogen column densities are susceptible to substantial ionization effects, making their abundance measurements unreliable (Jenkins 2009).

For Zn, Jenkins (2009) assumed the oscillator strengths from Morton (2003). However, the more recent depletion studies in the LMC and SMC used the newer, preferred oscillator strength from Kisielius et al. (2015). To homogenize the measurements, we therefore corrected the Zn column densities and depletions reported in Jenkins (2009) by −0.1 dex, which is the difference between the oscillator strengths for the Zn II $\lambda\lambda 2026, 2062$ transitions in Morton (2003) and Kisielius et al. (2015).

Table 4 of Jenkins (2009) provides the A_X , B_X , and z_X coefficients describing the relation between $\delta(X)$ and F_* for the Milky Way. We updated the zero-point B_{Zn} of this relation for Zn according to the correction performed on the depletion measurements, to account for the more recent oscillator strength for the Zn lines. The A_X , B_X , and z_X coefficients for the MW are summarized in Table 2. Last, the total abundances for the Milky Way are listed in Jenkins (2009) and summarized in Table 1.

Table 2
 A_X , B_X , and z_X Coefficients Relating Depletions and F_* in the MW, LMC, and SMC

Element	A_X			B_X			z_X		
	MW	LMC	SMC	MW	LMC	SMC	MW	LMC	SMC
C	-0.10 ± 0.23	-0.19 ± 0.06	0.803
O	-0.23 ± 0.05	-0.14 ± 0.05	0.598
Mg	-1.00 ± 0.04	-0.60 ± 0.11	-0.25 ± 0.26	-0.80 ± 0.02	-0.50 ± 0.02	-0.33 ± 0.03	0.531	0.407	0.162
Si	-1.14 ± 0.06	-1.11 ± 0.12	-1.05 ± 0.09	-0.57 ± 0.03	-0.68 ± 0.03	-0.36 ± 0.02	0.305	0.247	0.129
S	-0.879 ± 0.28	-1.02 ± 0.10	-0.87 ± 0.14	-0.091 ± 0.04	-0.31 ± 0.02	-0.02 ± 0.04	0.290	0.137	0.106
Ti	-2.05 ± 0.06	-1.48 ± 0.15	-1.45 ± 0.09	-1.96 ± 0.03	-1.63 ± 0.02	-1.23 ± 0.02	0.430	0.401	0.189
Cr	-1.45 ± 0.06	-1.18 ± 0.08	-1.33 ± 0.16	-1.51 ± 0.06	-1.13 ± 0.02	-0.93 ± 0.02	0.470	0.368	0.155
Fe	-1.28 ± 0.04	-1.28 ± 0.04	-1.28 ± 0.07	-1.51 ± 0.03	-1.51 ± 0.03	-1.18 ± 0.02	0.437	0.437	0.181
Ni	-1.49 ± 0.06	-1.29 ± 0.08	-1.41 ± 0.14	-1.83 ± 0.04	-1.26 ± 0.02	-1.11 ± 0.02	0.599	0.338	0.141
Cu	-0.71 ± 0.09	-1.15 ± 0.42	...	-1.10 ± 0.06	-0.44 ± 0.09	...	0.711	0.325	...
Zn	-0.61 ± 0.07	-0.73 ± 0.07	-0.51 ± 0.14	-0.38 ± 0.04	-0.36 ± 0.02	-0.31 ± 0.02	0.555	0.358	0.168

2.2. Large Magellanic Cloud

In the LMC, Roman-Duval et al. (2021) recently obtained gas-phase abundances and depletions for a large sample of sight lines observed with HST/STIS and COS as part of the METAL (GO-14675) large program (Roman-Duval et al. 2019). The study includes most of the major constituents of dust and other heavy elements commonly used as metallicity tracers (Mg, Si, S, Cr, Fe, Ni, Cu, Zn, and Ti), but not C and O, for which UV transitions are either too saturated or too weak to be detected in the LMC. With 32 sight lines with measured depletions for most of the elements listed above toward each sight line, this is the most comprehensive sample available in this galaxy, and the one we use in this analysis. As for the MW, we only retain detections (not limits). The column density, abundance, and depletion measurements, along with the sight-line hydrogen column density, are listed in Table 5 of Roman-Duval et al. (2021).

We note that Tchernyshyov et al. (2015) measured depletions toward a common sample of LMC sight lines with FUSE and COS/NUV. Since the spectral resolution of STIS, predominantly used in the Roman-Duval et al. (2021) study, is superior to the spectral resolution of both COS/NUV and FUSE, and since the Tchernyshyov et al. (2015) sample is included in the Roman-Duval et al. (2021) sample, we do not make use of their results in this analysis. Nonetheless, Roman-Duval et al. (2021) did perform a comparison of the depletions obtained by both studies and found them to be in general agreement, within errors.

The A_X , B_X , and z_X coefficients for the LMC are not directly available in Roman-Duval et al. (2021). Indeed, since the F_* scale is tied to the particular sight lines used to anchor the $F_* = 0$ and 1 extremes, it is not possible to use the same normalizations of the F_* scale in galaxies other than the MW. Therefore, similar to the computation of F_* in SMC by Jenkins & Wallerstein (2017), the F_* parameter in the LMC is given by

$$F_* = \frac{\delta(\text{Fe}) - B_{\text{Fe}}}{A_{\text{Fe}}} + z_{\text{Fe}}, \quad (3)$$

where $A_{\text{Fe}} = -1.285$, $B_{\text{Fe}} = -1.513$, and $z_{\text{Fe}} = 0.437$ are the coefficients of the linear relation between $\delta(\text{Fe})$ and F_* in the Milky Way given in Table 4 of Jenkins (2009). Fe was chosen to tie the F_* scale in different galaxies because Fe depletions can generally be derived easily for all sight lines. Then, we combine Equation (3) and the relation between $\delta(\text{Fe})$ and $\delta(X)$, of the form $\delta(X) = a_X(\delta(\text{Fe}) - \zeta_X) + b_X$, given in Table 7 of

Roman-Duval et al. (2021) to compute A_X , B_X , and z_X . We note that ζ_X corresponds to z_X in Table 7 of Roman-Duval et al. (2021).

$$A_X = -1.285a_X, \quad (4)$$

$$B_X = b_X, \quad (5)$$

$$z_X = -\frac{\zeta_X + 0.951}{1.285}. \quad (6)$$

The A_X , B_X , and z_X coefficients for the LMC are given in Table 2. Total abundances assumed to derive depletions in the LMC are identical to those used in Roman-Duval et al. (2021) and are listed in Table 1. In particular, abundances for all elements except S, Ti, and Cu were taken from Tchernyshyov et al. (2015), who used a statistical technique to combine disparate measurements of stellar abundances in the Magellanic Clouds. Tchernyshyov et al. (2015) did not include S, Ti, and Cu, and abundances for those elements were taken from different publications (see Table 1).

2.3. Small Magellanic Cloud

Depletions for nine elements (Mg, Si, S, Cr, Fe, Ni, Cu, Zn, and Ti) were obtained by Jenkins & Wallerstein (2017) toward 18 stars in the SMC observed with HST/STIS. We use these measurements in our analysis. The column density, abundance, and depletion measurements, along with sight-line information such as $\log N(\text{H I})$, $\log N(\text{H}_2)$ are given in their Table 3.

As for the LMC, Tchernyshyov et al. (2015) obtained depletions for 13 stars in the SMC. Eight of those sight lines were observed with COS/NUV, yielding depletions for Si, Zn, Cr, Fe, and P. Of those eight stars, four were reobserved with STIS by Jenkins & Wallerstein (2017), which resulted in more accurate measurements for Si, Zn, Cr, and Fe and new measurements for other elements (e.g., Mg). The other five SMC sight lines from Tchernyshyov et al. (2015) were observed with FUSE, providing depletions for Fe and P only. Since our analysis relies on samples with the full set of depletions measurements, including the major constituents of dust such as Mg, Si, Fe, and Ni, as well as commonly used metallicity and depletion tracers such as S and Zn, we do not include the depletion measurements from Tchernyshyov et al. (2015), which targeted a smaller subset of elements.

Jenkins & Wallerstein (2017) estimated F_* following Equation (3), with the resulting F_* values for the SMC sight lines listed in their Table 5. The A_X , B_X , and z_X for the SMC are given in their Table 6, and summarized in our Table 2. When

available, we assume the same total abundances as Jenkins & Wallerstein (2017) for the SMC (their Table 2).

Jenkins & Wallerstein (2017) did not include C and O, and for those elements we assume total abundances from Tchernyshyov et al. (2015). Total abundances for the SMC and associated references are summarized in Table 1.

3. The Collective Behavior of Depletions in the MW, LMC, and SMC

3.1. Constraints from MW, LMC, and SMC Measurements

In their large sample of depletions obtained in the Milky Way, Jenkins (2009) established that depletions for different elements tightly correlate with each other, and that the collective advancement of depletions for all elements can be described by the parameter F_* . In this section, we examine the relations between depletions of different elements in the Milky Way, LMC, and SMC. These relations are shown in Figure 1, where both the depletion measurements for several elements are shown as a function of Fe depletions, in all three galaxies. Also shown are the fitted relations obtained from the A_X , B_X , and z_X coefficients (Table 2).

We note that a vertical displacement of the relations $\delta(X)-\delta(\text{Fe})$ between the MW, LMC, and SMC could simply be due to differences and/or uncertainties on the assumed total abundances. However, differences in their slopes will reflect real differences in the rates at which elements deplete from the gas to the dust phase.

For most elements (Si, S, Ni, Zn, and Cr), the relation between depletions of X and Fe does not significantly change between the MW, LMC, and SMC. The invariance of the $\delta(X)-\delta(\text{Fe})$ relation with metallicity, at least over the 0.2–1 Z_\odot range, implies that Fe, the interstellar abundance and depletion of which are straightforward to measure in UV spectra thanks to its numerous transitions with a range of oscillator strengths, can be used as a proxy for the depletions of other elements that are more difficult to measure.

However, there are appreciable differences in the $\delta(X)-\delta(\text{Fe})$ relations between the MW, LMC, and SMC for Mg, Ti, and more marginally, Cu. Depletions of Cu are only measured for a small sample of sight lines in the MW and LMC, with a high fraction of LMC sight lines having only upper limits. As a result, the relatively large difference in the $\delta(\text{Cu})-\delta(\text{Fe})$ between the MW and LMC is not statistically significant (1σ difference). However, for Mg, the slopes differ at the 4σ level between the MW and the LMC, and at the 3σ level between the MW and the SMC, a decrease in the steepness of the relation with decreasing metallicity that is clearly seen in Figure 1. For Ti, the LMC and SMC relations are in almost perfect agreement, but differ from the MW relation at the 3σ level. Mn was not measured in the LMC as part of METAL, but Jenkins & Wallerstein (2017) report significant differences between the rate of depletion of Mn in the SMC and MW. To explain differences in the depletion rates between different galaxies, Jenkins & Wallerstein (2017) offered the conjecture that the lower abundance of C in the SMC and the consequences of the mix of PAH and silicates could influence the chemical affinities of various atoms to dust and hence their respective rates of depletions.

3.2. Abundance Ratios in the MW, LMC, and SMC

In nearby galaxies, total (gas+dust) abundances in the ISM can be estimated indirectly from the photospheric abundances

of young stars recently formed out of the ISM. In more distant systems such as DLAs, depletions can only be inferred from abundance ratios of volatile to refractory elements, which are heavily influenced by their different rates of depletion. Thus, comparing the relations between different abundance ratios in the MW, LMC, and SMC can reveal key information about the depletion process in both local galaxies and more distant systems.

We examine the relation between abundance ratios involving volatile elements Zn and S in the MW, LMC, and SMC. This is similar to the comparison performed by De Cia (2018), but with the addition of the new LMC sample obtained from the METAL program. In Figures 3 and 2, we show various abundance ratios ($[X/\text{Zn}]$ and $[X/\text{S}]$, respectively, for $X = \text{Mg}, \text{Si}, \text{S}, \text{Ti}, \text{Cr}, \text{Fe},$ and Ni) in the MW, LMC, and SMC as a function of $[\text{Zn}/\text{Fe}]$, which is commonly used as a depletion tracer in DLAs. For the MW, LMC, and SMC, both the abundance ratios toward individual sight lines and the relations derived from the A , B , and z coefficients relating depletions and F_* (and hence relating depletions of different elements) are shown in Figures 2 and 3. We note that, while plotted as independent (orthogonal) in x and y , error bars in Figures 2 and 3 should not be orthogonal when the same element is involved in both axes.

Because depletions cannot exceed the zero value, the relations between abundance ratios derived from the A , B , and z coefficients are not simple linear functions. The abundance ratio $[X/Y]$ is determined by the depletions and α -enhancement of X and Y via

$$\left[\frac{X}{Y}\right] = \delta(X) - \delta(Y) + \alpha(X) - \alpha(Y), \quad (7)$$

where $\alpha(X)$ is the over- or underabundance of X with respect to Fe relative to the solar $(X/\text{Fe})_\odot$ ratio ($\alpha(X) = [X/\text{Fe}]$, where $[X/\text{Fe}]$ is measured in stars). We note that $\alpha(X)$ refers to abundance variations relative to solar in stars, where dust depletion effects are not occurring. In particular, $\alpha(X)$ accounts for nucleosynthetic effects in α -elements (e.g., Si, S, and Mg). α is known from the stellar abundances in the LMC and SMC listed in Table 1 ($\alpha = 0$ in the MW by construction). The depletion of X is $\delta(X) = A_X(F_* - z_X) + B_X$. The value of $\delta(X)$ is capped at zero. This results in $[X/Y]$ following the piecewise linear functions shown in Figures 2 and 3 in the MW, LMC, and SMC.

The abundance ratios shown in Figures 2 and 3 are generally in reasonable agreement between the MW, LMC, and SMC. This is not surprising in light of Figure 1, since abundance ratios depend primarily on the relative depletions of the elements involved, and Figure 1 shows that the relation between the depletions of different elements remains relatively constant between the MW, LMC, and SMC. The invariance of the relation between abundance ratios between the MW, LMC, and SMC implies that abundance ratios should in principle serve as accurate tracers of depletions in DLAs, at least down to the 20% solar metallicity probed by local studies. Deriving calibrations of abundance ratios, in particular $[\text{Zn}/\text{Fe}]$, in the MW, LMC, and SMC to be used by the DLA community will be the subject of the METAL IV paper (J. Roman-Duval et al. 2022, in preparation).

As in Figure 1, Mg (in the SMC) and Ti (in the MW) are the only exceptions to the invariance of abundance ratio variations between the MW, LMC, and SMC, deviating slightly from the

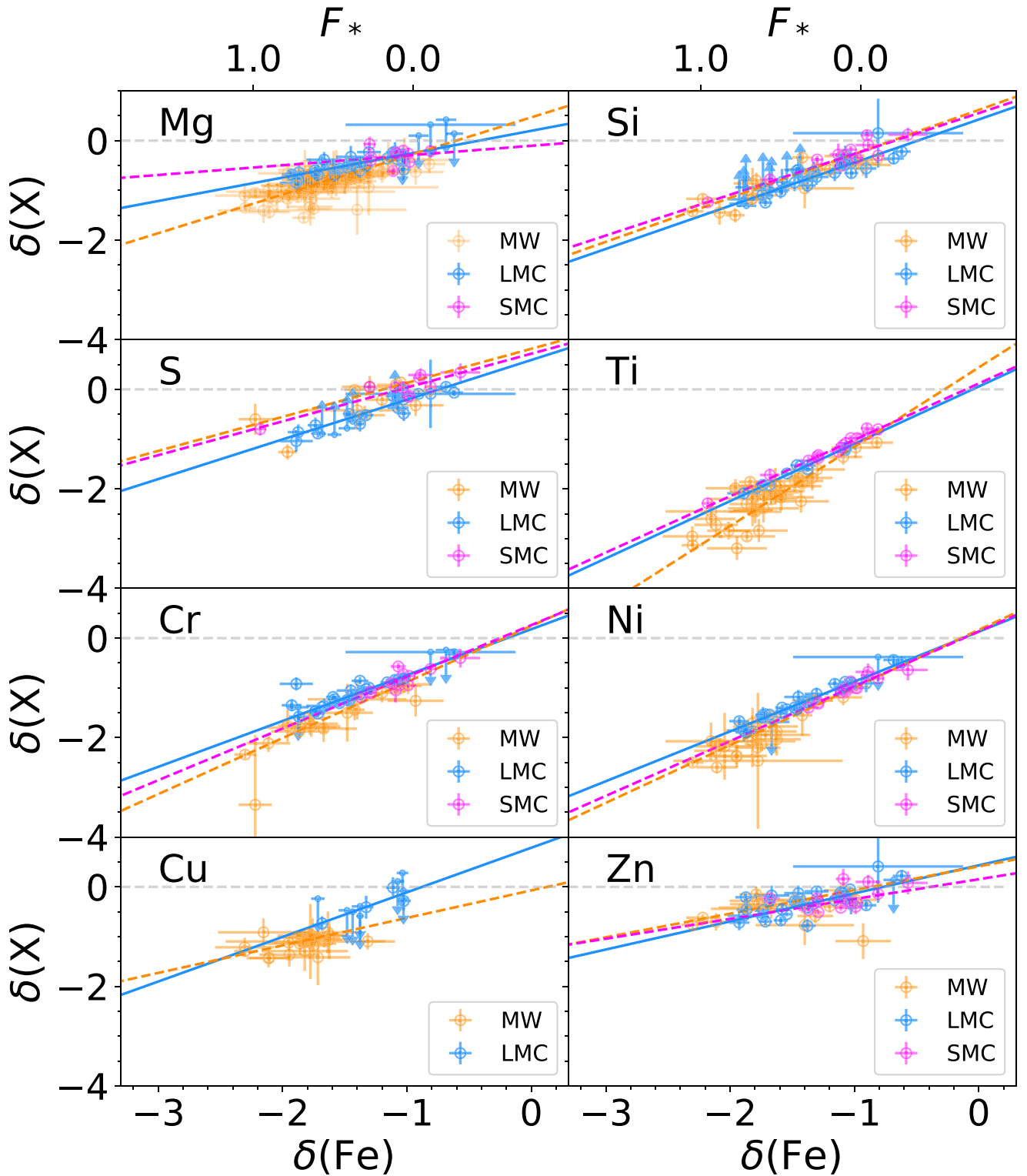


Figure 1. Depletions (log fraction in the gas phase) for Mg, Si, S, Cr, Ni, Cu, Zn, and Ti as a function of iron depletions ($\delta(\text{Fe})$). The fits of the depletions are shown by the colored lines (see Equation (2) with coefficients given in Table 2). Orange, blue, and magenta correspond to the Milky Way (Jenkins 2009), LMC (Roman-Duval et al. 2021), and SMC (Jenkins & Wallerstein 2017), respectively.

other trends. For Mg, some of the rather large differences seen between the fits obtained in the MW and the SMC (and, to some extent, the LMC) at high $[\text{Zn}/\text{Fe}]$ may be due to the limited dynamic range and small sample in depletion measurements, resulting in the diverging extrapolation of the fit at high $[\text{Zn}/\text{Fe}]$.

3.3. Estimating C and O Depletions in the LMC and SMC

The full suite of elements that make up most of the dust mass does not necessarily have depletion measurements in all three galaxies. In particular, C and O in the LMC and SMC are not measured because the UV transitions of C and O are either too

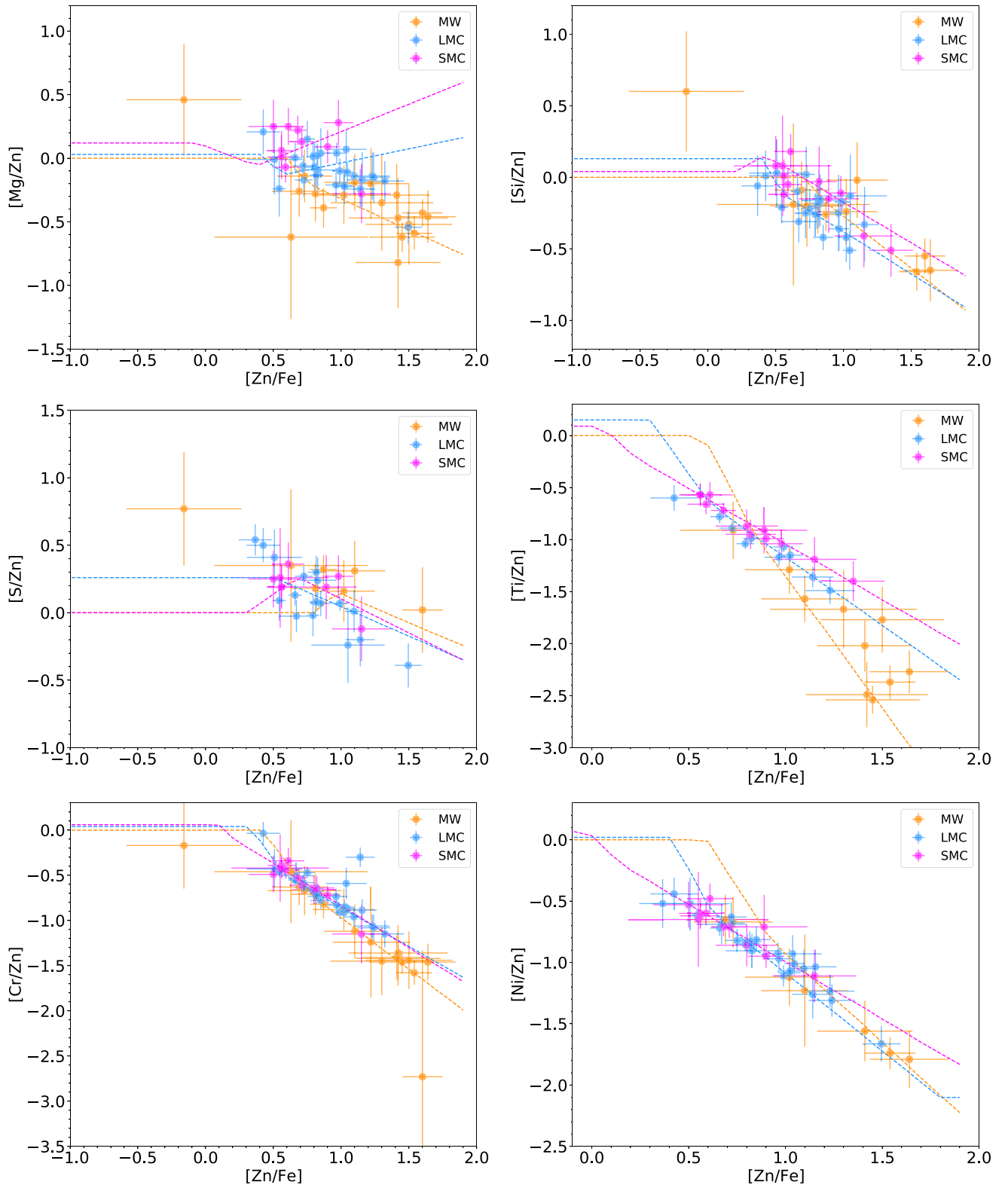


Figure 2. Relation between abundance ratios $[X/Zn]$ with $X = \text{Mg}, \text{Si}, \text{S},$ and Cr in the MW (orange), LMC (blue), and SMC (magenta). The dashed lines are obtained from the relation between depletions of different elements in the MW, LMC, and SMC (see Equation (2), Table 2, and Figure 1).

saturated or too weak. Unfortunately, C and O constitute the largest mass reservoir of heavy elements that can be included in dust. This limitation can be circumvented thanks to the relative invariance of the collective behavior of depletions observed in the MW, LMC, and SMC. Here, as in Roman-Duval et al. (2021,

their Section 7), we therefore use the assumption that the relation between C or O depletions and iron depletions behaves similarly in the Milky Way, LMC, and SMC, as is the case for other elements. Knowing the iron depletions for all our sight lines in all three galaxies, we apply the known MW relation between $\delta(\text{C})$ or

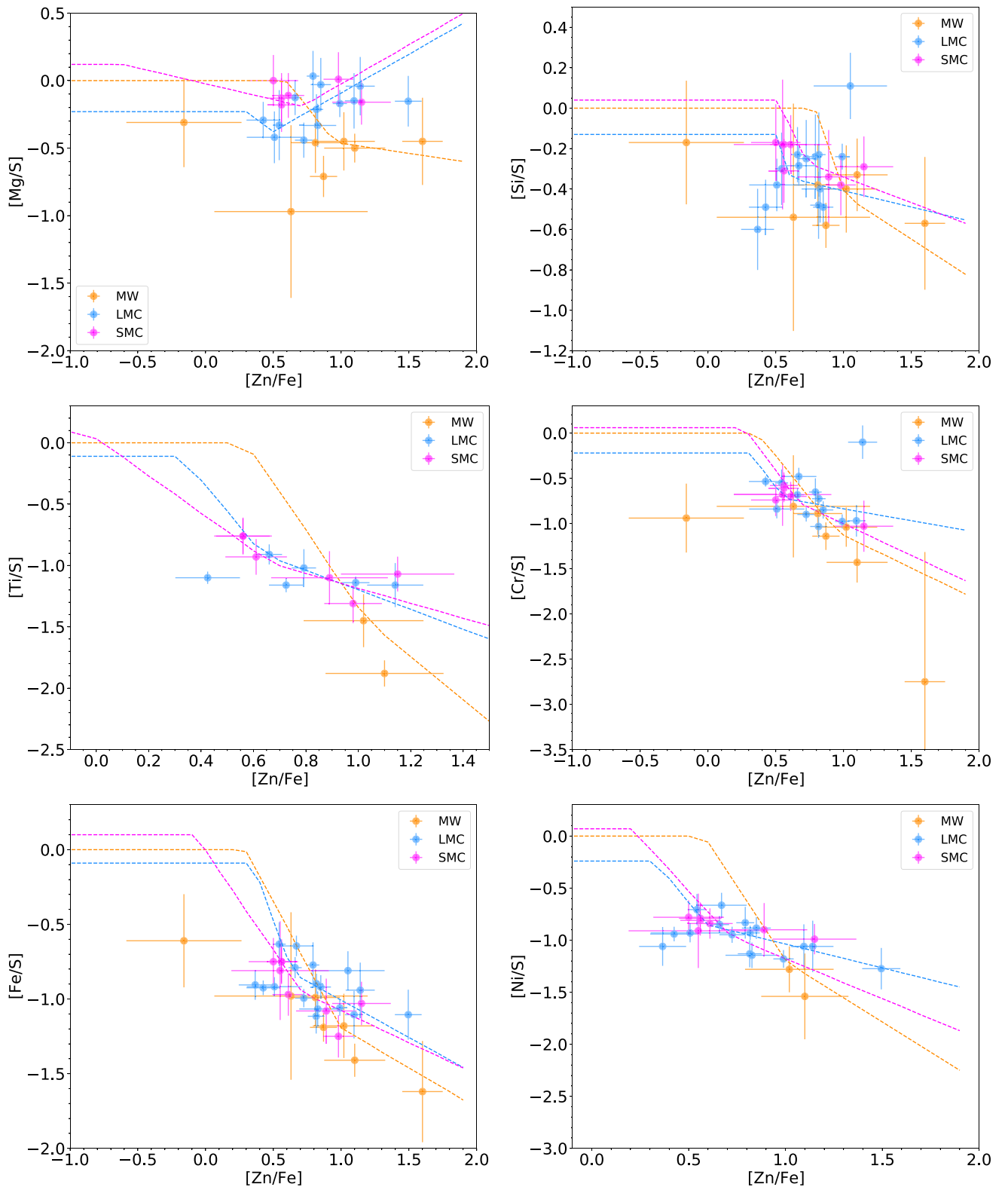


Figure 3. Relation between abundance ratios $[X/S]$ with $X = \text{Mg}, \text{Si}, \text{Fe},$ and Cr in the MW (orange), LMC (blue), and SMC (magenta). The dashed lines are obtained from the relation between depletions of different elements in the MW, LMC, and SMC (see Equation (2), Table 2, and Figure 1).

$\delta(\text{O})$ and $\delta(\text{Fe})$ (Equation (2) and coefficients in Table 2) from Jenkins (2009) to obtain an estimate of $\delta(\text{C})$ or $\delta(\text{O})$ for each sight line. The errors on the A_X and B_X coefficients are propagated through the calculation of C and O depletions.

We note that a deficiency of carbon relative to other elements in the LMC ($\log \text{C}/\text{O} = -0.56$ in the LMC versus -0.30 in the MW, and -0.62 in the SMC) may potentially affect the rate of carbon depletions compared to those of other elements. For

example, the fraction of carbonaceous dust and PAHs relative to silicates is different between the MW, LMC, and SMC (Chastenet et al. 2019), which could be attributed to the different chemical affinities of dust compounds induced by the lower carbon abundance in the LMC and SMC compared to the MW.

4. The Dust-to-gas and Dust-to-metal Ratios

With depletions in hand for a suite of elements in the MW, LMC, and SMC, we can derive the dust-to-gas and dust-to-metal ratios toward each sight line by summing the mass-weighted dust-phase abundance of all elements:

$$D/G = \frac{1}{1.36} \sum_X (1 - 10^{\delta(X)}) \left(\frac{N(X)}{N_H} \right)_{\text{tot}} W(X) \quad (8)$$

and

$$D/M = \frac{\sum_X (1 - 10^{\delta(X)}) \left(\frac{N(X)}{N_H} \right)_{\text{tot}} W(X)}{\sum_X \left(\frac{N(X)}{N_H} \right)_{\text{tot}} W(X)}, \quad (9)$$

where $(N(X)/N_H)_{\text{tot}}$ is the total abundance of element X in the galaxy (MW, LMC, or SMC), assumed to be that of stellar photospheres of young stars, and $W(X)$ is the atomic weight of element X. Throughout this paper, when depletions are estimated from the A_X , B_X , and z_X coefficients, errors on these coefficients are propagated—for example, through the calculation of D/G and D/M.

5. The Relation between Depletions, D/M, D/G, and Hydrogen Column Density in the MW, LMC, and SMC

5.1. Relation between Depletions and Hydrogen Column Density

Based on the METAL spectra, Roman-Duval et al. (2021) investigated the physical parameters driving the depletion levels in the LMC, and found that the hydrogen column density was the primary parameter correlated with the depletions of different elements. In a face-on disk galaxy such as the LMC, this is consistent with the gas density being a determining factor in the depletion levels. Indeed, variations in the column density stem from variations either in the density or in the path length. The latter result from variations of the scale height of the gas perpendicular to the plane of the LMC, the magnitude of which are smaller compared to variations in the density. Therefore, the hydrogen column density should be a direct tracer of the average gas density along the line of sight. Of course, the average density itself will result from gas at a range of densities where depletions occur at correspondingly varying rates, and our measurements therefore reflect the average depletion behavior in the interstellar gas density structure.

In this section, we investigate whether depletion measurements in the MW and SMC also support the gas density and column density being the main parameters driving depletion levels in the ISM, and if so, whether the trends between depletions and $\log N(\text{H})$ are consistent with those observed in the LMC.

The depletions for all elements measured in the MW, LMC, and SMC are shown as a function of $\log N(\text{H})$ in Figure 4. For all galaxies and elements, there is a clear anticorrelation between $\delta(X)$ and $\log N(\text{H})$: as the column density increases, an

increasing fraction of metals are locked into dust grains (recall that depletions correspond to the log fractions of metals in the gas). As a result, even for volatile elements such as S and Zn often used as metallicity tracers in DLAs, the depletion level can exceed -0.5 dex for $\log N(\text{H}) > 21 \text{ cm}^{-2}$, even at 20% solar metallicity.

We fit the relation between depletions and $\log N(\text{H})$ using linear functions, as in Roman-Duval et al. (2021):

$$\delta(X) = B_H(X) + A_H(X)(\log N(\text{H}) - \log N_{H_0}(X)), \quad (10)$$

which has the same form as Equation (2), but is applicable to $N(\text{H})$ instead of F_* . The parameter $N_{H_0}(X)$ is introduced to remove the covariance between errors on the slope, $A_H(X)$, and intercept, $B_H(X)$, of the relation, and is given by

$$\log N_{H_0}(X) = \frac{\sum_{\log} \frac{\log N(H)}{\sigma(\delta(X))^2}}{\sum_{\log} \frac{1}{\sigma(\delta(X))^2}}. \quad (11)$$

The resulting $A_H(X)$, $B_H(X)$, and N_{H_0} parameters for the MW, LMC, and SMC are listed in Table 3 and shown in Figure 4. The coefficients for the LMC were computed in Roman-Duval et al. (2021) and are repeated here for easy comparison with the MW and SMC. For the MW, where depletions are measured for sight lines with $\log N(\text{H})$ down to 18 cm^{-2} , we only fit $\delta(X)$ versus $\log N(\text{H})$ in the range $\log N(\text{H}) = 20\text{--}22 \text{ cm}^{-2}$, so as to be consistent with the LMC and SMC, where only sight lines with $\log N(\text{H}) > 20 \text{ cm}^{-2}$ were measured. Precomputed values of depletions for $\log N(\text{H}) = 20, 21, \text{ and } 22 \text{ cm}^{-2}$ in the MW, LMC, and SMC are listed in Table 4 for convenience. Those values are computed from Equation (10) and the coefficients listed in Table 3.

In Table 4, we also list estimates of C and O depletions obtained using the approach described in Section 3.3, which relies on the invariance of the collective behavior of depletions between the MW, LMC, and SMC. For a given $\log N(\text{H})$, we use Equation (10) and the coefficients listed in Table 3 to estimate the Fe depletion. We then make use of the MW relation between the depletions of Fe and C or O (Equation (2) and coefficients in Table 2) to estimate $\delta(\text{C})$ and $\delta(\text{O})$ in the LMC and SMC. This allows us to compute the D/M in all three galaxies, from the depletions listed in Table 4 and Equation (9).

5.2. Relation between D/G and Hydrogen Column Density

Applying Equation (8) to the depletion measurements of Mg, Si, S, Cr, Fe, Ni, Zn, and Ti, as well as the estimation of depletions for C and O, we obtain the relation between D/G and column density shown in the top panels of Figures 5, 6, and 7 for the MW, LMC, and SMC, respectively. In those figures, we plot both the D/G computed for individual sight lines (points) and the relation between D/G and $\log N(\text{H})$ derived from the fits of depletions to $\log N(\text{H})$ given in Table 3 (lines). Errors on the $A_H(X)$ and $B_H(X)$ coefficients are included in the calculation of the fitted relation between D/G and $\log N(\text{H})$.

In all three galaxies, and consistent with the trends we observe for depletions of individual elements, the depletion-based D/G increases with increasing hydrogen column density. Between $\log N(\text{H}) = 20$ and 22 cm^{-2} , the increase in D/G represents a factor of two in the MW, four in the LMC, and five in the SMC.

The observed trend of D/G versus $\log N(\text{H})$ is consistent with the theoretical expectation that gas-phase metals accrete

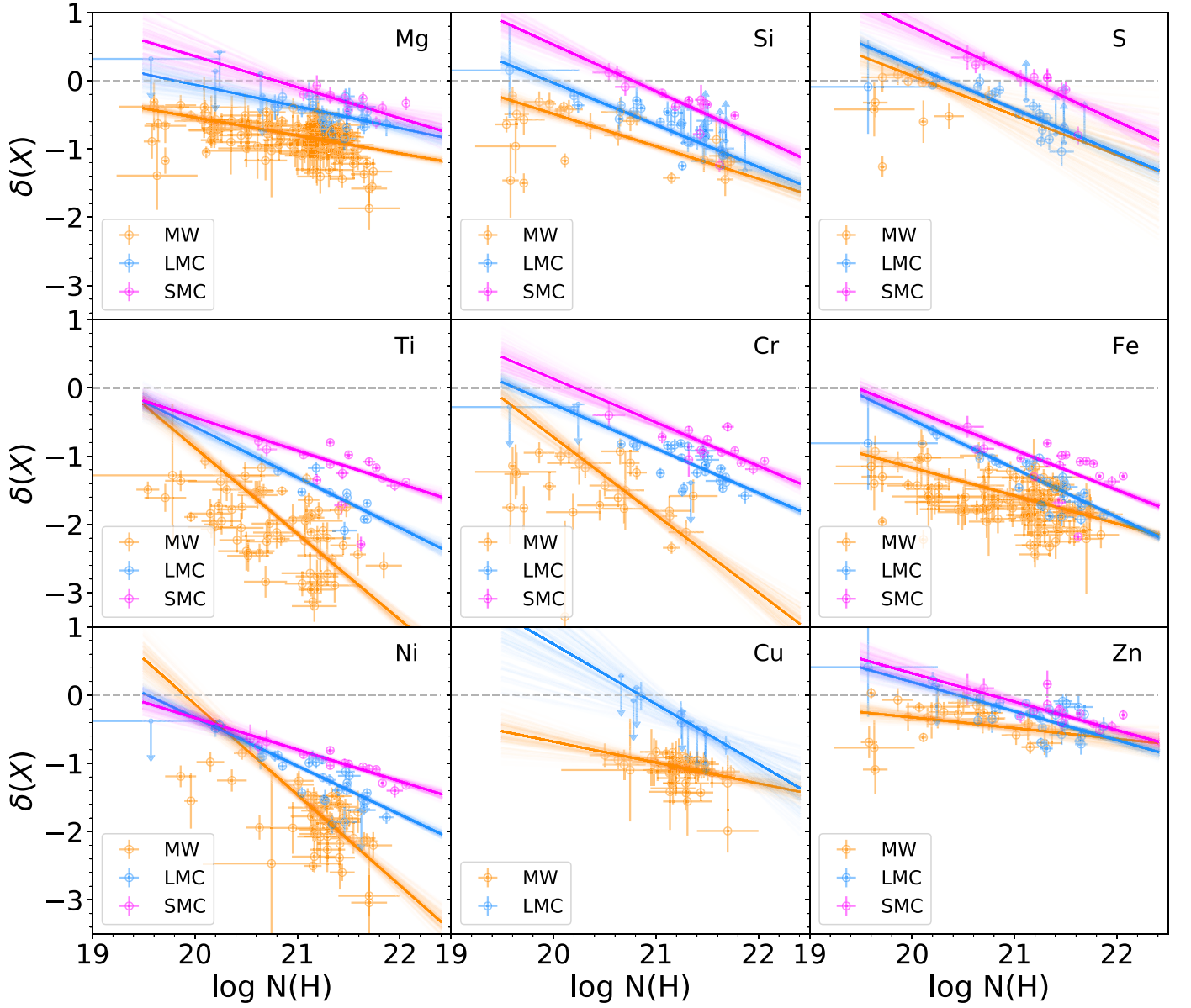


Figure 4. Depletions (log fraction in the gas phase) for Mg, Si, S, Cr, Fe, Ni, Cu, Zn, and Ti, as a function of $\log N(\text{H})$. Orange, blue, and magenta correspond to the Milky Way (Jenkins 2009), LMC (Roman-Duval et al. 2021), and SMC (Jenkins & Wallerstein 2017), respectively. The fraction of metals in the gas phase decreases with increasing column density. Different realizations of the fits are shown with transparencies computed as the square root of the likelihood of each realization.

Table 3
 $A_{\text{H}}(X)$, $B_{\text{H}}(X)$, and $\log N_{\text{H}0}(X)$ Coefficients Relating Depletions and $\log N(\text{H})$ in the MW, LMC, and SMC

Element	$A_{\text{H}}(X)$			$B_{\text{H}}(X)$			$\log N_{\text{H}0}(X)$		
	MW	LMC	SMC	MW	LMC	SMC	MW	LMC	SMC
C	0.12 ± 0.12	-0.14 ± 0.04	21.340
O	-0.03 ± 0.05	-0.15 ± 0.01	21.265
Mg	-0.26 ± 0.03	-0.32 ± 0.09	-0.45 ± 0.14	-0.83 ± 0.01	-0.50 ± 0.02	-0.32 ± 0.04	21.121	21.374	21.490
Si	-0.47 ± 0.05	-0.61 ± 0.07	-0.68 ± 0.08	-0.81 ± 0.03	-0.67 ± 0.03	-0.36 ± 0.03	20.682	21.040	21.308
S	-0.58 ± 0.22	-0.64 ± 0.06	-0.69 ± 0.12	-0.03 ± 0.05	-0.32 ± 0.02	-0.02 ± 0.04	20.171	20.842	21.166
Ti	-1.26 ± 0.08	-0.74 ± 0.07	-0.48 ± 0.06	-2.03 ± 0.03	-1.63 ± 0.02	-1.15 ± 0.02	20.916	21.427	21.490
Cr	-1.14 ± 0.13	-0.65 ± 0.04	-0.64 ± 0.09	-1.60 ± 0.05	-1.14 ± 0.01	-0.90 ± 0.02	20.769	21.383	21.618
Fe	-0.41 ± 0.03	-0.71 ± 0.03	-0.59 ± 0.04	-1.62 ± 0.02	-1.39 ± 0.01	-1.18 ± 0.01	21.097	21.288	21.469
Ni	-1.33 ± 0.11	-0.71 ± 0.04	-0.46 ± 0.06	-1.77 ± 0.03	-1.26 ± 0.01	-1.04 ± 0.02	21.232	21.318	21.527
Cu	-0.30 ± 0.10	-0.88 ± 0.30	...	-1.08 ± 0.02	-0.44 ± 0.09	...	21.293	21.354	...
Zn	-0.16 ± 0.07	-0.43 ± 0.04	-0.42 ± 0.07	-0.42 ± 0.03	-0.36 ± 0.01	-0.32 ± 0.02	20.588	21.299	21.543

Table 4
Depletion and D/M Values Obtained from Linear Fits to Hydrogen Column Density for $\log N(\text{H}) = 20, 21,$ and 22 cm^{-2}

	$\log N(\text{H}) = 20 \text{ cm}^{-2}$			$\log N(\text{H}) = 21 \text{ cm}^{-2}$			$\log N(\text{H}) = 22 \text{ cm}^{-2}$		
	MW	LMC	SMC	MW	LMC	SMC	MW	LMC	SMC
$\delta(\text{C})$	-0.13 ± 0.16	-0.07 ± 0.28	-0.06 ± 0.30	-0.16 ± 0.09	-0.13 ± 0.15	-0.11 ± 0.19	-0.19 ± 0.06	-0.19 ± 0.06	-0.16 ± 0.10
$\delta(\text{O})$	-0.05 ± 0.06	0.00 ± 0.07	0.00 ± 0.08	-0.12 ± 0.05	-0.05 ± 0.06	-0.00 ± 0.06	-0.19 ± 0.05	-0.18 ± 0.05	-0.11 ± 0.05
$\delta(\text{Mg})$	-0.54 ± 0.04	-0.06 ± 0.12	0.00 ± 0.21	-0.80 ± 0.01	-0.38 ± 0.04	-0.09 ± 0.08	-1.07 ± 0.03	-0.70 ± 0.06	-0.55 ± 0.08
$\delta(\text{Si})$	-0.49 ± 0.05	-0.03 ± 0.08	0.00 ± 0.11	-0.96 ± 0.04	-0.65 ± 0.03	-0.15 ± 0.04	-1.44 ± 0.08	-1.26 ± 0.07	-0.84 ± 0.06
$\delta(\text{S})$	0.00 ± 0.06	0.00 ± 0.05	0.00 ± 0.15	-0.51 ± 0.19	-0.42 ± 0.02	0.00 ± 0.05	-1.09 ± 0.41	-1.05 ± 0.07	-0.59 ± 0.11
$\delta(\text{Ti})$	-0.88 ± 0.07	-0.57 ± 0.09	-0.43 ± 0.08	-2.14 ± 0.03	-1.31 ± 0.03	-0.92 ± 0.03	-3.40 ± 0.09	-2.05 ± 0.04	-1.40 ± 0.03
$\delta(\text{Cr})$	-0.72 ± 0.11	-0.24 ± 0.06	0.00 ± 0.14	-1.86 ± 0.06	-0.89 ± 0.02	-0.50 ± 0.06	-3.00 ± 0.16	-1.54 ± 0.03	-1.14 ± 0.04
$\delta(\text{Fe})$	-1.17 ± 0.04	-0.47 ± 0.04	-0.32 ± 0.06	-1.58 ± 0.02	-1.18 ± 0.01	-0.91 ± 0.02	-1.99 ± 0.03	-1.89 ± 0.02	-1.49 ± 0.03
$\delta(\text{Ni})$	-0.13 ± 0.14	-0.33 ± 0.05	-0.33 ± 0.10	-1.46 ± 0.04	-1.04 ± 0.02	-0.80 ± 0.04	-2.79 ± 0.09	-1.75 ± 0.03	-1.26 ± 0.03
$\delta(\text{Zn})$	-0.33 ± 0.05	0.00 ± 0.06	0.00 ± 0.12	-0.48 ± 0.04	-0.23 ± 0.02	-0.10 ± 0.05	-0.64 ± 0.10	-0.66 ± 0.03	-0.51 ± 0.04
D/M	0.30 ± 0.08	0.12 ± 0.11	0.08 ± 0.14	0.43 ± 0.06	0.34 ± 0.07	0.16 ± 0.10	0.52 ± 0.04	0.52 ± 0.05	0.40 ± 0.06

Notes. For C and O, we estimate depletions by applying the MW relation between Fe and C or O depletion (see Section 3.3). Depletions are capped at zero, resulting in some 0.00 values in the fits of depletions vs. $\log N(\text{H})$, particularly at low column density and for volatile elements.

onto dust grains at higher rates in higher-density environments, as explained in Asano et al. (2013) for example: the timescale for dust growth in the ISM is inversely proportional to density. The correlation between depletions (or D/G) versus $\log N(\text{H})$ has more scatter in the MW than in the LMC and SMC, presumably due to the effects of varying path lengths in the MW. Indeed, sight lines in the MW go through a longer, varying path in the disk, while sight lines in the LMC and SMC probe gas and dust in their disks face-on (to a lesser extent in the SMC, owing to its ‘‘cigar’’ shape, although Yanchulova Merica-Jones et al. (2021) demonstrate that gas in the SMC constitutes a thin layer). In the LMC, and to a lesser extent the SMC, variations in the path length are driven by changes in the scale height of the gas perpendicular to the plane of those galaxies. The magnitudes of such variations are probably small compared to the variation of $N(\text{H})$ in the ISM of these galaxies. Hence, $\log N(\text{H})$ should be a good proxy for the average $n(\text{H})$ over the entire line of sight to a star embedded near the plane of the LMC or SMC. On the other hand, the path length of a line of sight in the MW can vary considerably depending on the distance to the background star, and $\log N(\text{H})$ does not trace the mean density along the line of sight, resulting in more scatter in the relation between depletions and $\log N(\text{H})$. Correspondingly, in the case of the MW, where the path length through the ISM d can be determined, Jenkins (2009) showed that depletions (through F_*) correlate much better with $N(\text{H})/d$ than with $N(\text{H})$.

In the LMC and SMC, D/G is also measured from FIR emission in Roman-Duval et al. (2014, 2017), particularly as a function of $\log N(\text{H})$ in the latter study, and we plot these trends in Figures 6 and 7 for comparison with the depletion-based D/G measurements. This comparison for the LMC was discussed in Roman-Duval et al. (2021): the FIR-based D/G is a factor of two lower than the depletion-based D/G, but the slopes of D/G versus $\log N(\text{H})$ are similar for both types of measurements. In the SMC, the FIR-based D/G is a factor of three lower than the depletion-based D/G for $\log N(\text{H}) > 20.5 \text{ cm}^{-2}$, but the discrepancy is larger (factor of ~ 5) at lower column densities. The possible explanations for this discrepancy are presented in Section 7.4.

6. The Dust Composition Inferred from Depletions

Depletion measurements provide some clue as to the composition of dust in the MW, LMC, and SMC. Indeed, the fraction of the dust mass contributed by each element X, D_X , is given by

$$D_X = \frac{\left(1 - 10^{\delta(X)}\right) \left(\frac{N(X)}{N_{\text{H}}}\right)_{\text{tot}} W(X)}{1.36(D/G)}, \quad (12)$$

where $\delta(X)$ are the depletions, and $(N(X)/N_{\text{H}})_{\text{tot}}$ and $W(X)$ are the same terms as in Equation (8). D_X for the elements measured in the samples is shown in the bottom panels of Figures 5, 6, and 7 for the MW, LMC, and SMC, respectively. Not surprisingly, the dust mass is dominated by C, O, Mg, Si, Fe, and to a lesser extent at the highest column densities, S. In the MW, the dust mass budget is roughly equally split between C, O, Mg, Si, and Fe. However, as the metallicity decreases from the MW to the LMC and SMC, the contributions of Mg, Si, and O kick in at increasingly higher hydrogen column densities, roughly $\log N(\text{H}) \sim 20.5 \text{ cm}^{-2}$ in the LMC and 21 cm^{-2} in the SMC.

To visualize the dust composition in the MW, LMC, and SMC more effectively, bar plots of the dust mass fraction contributed by C, O, Mg, Si, and Fe are shown as a function of $\log N(\text{H})$ in each galaxy in Figures 8 and 9. Additionally, the fraction of the dust mass contributed by these elements in known condensates such as olivine, enstatite, or iron carbide are shown for comparison. No single condensate matches the observed composition of dust in the MW, LMC, or SMC, indicating a mix of different dust types is present in those galaxies. However, carbonaceous grains and iron carbide must dominate the dust mass at low column densities in the LMC (below $\log N(\text{H}) = 20.5 \text{ cm}^{-2}$) and SMC (below $\log N(\text{H}) = 21 \text{ cm}^{-2}$), while the contribution from silicates increases with increasing column density in those galaxies. This would be in line with the dust properties observed in the LMC and SMC using the FIR (Chasten et al. 2017), where carbon dust is observed to dominate, as evidenced by the spectral emissivity index of the FIR SED.

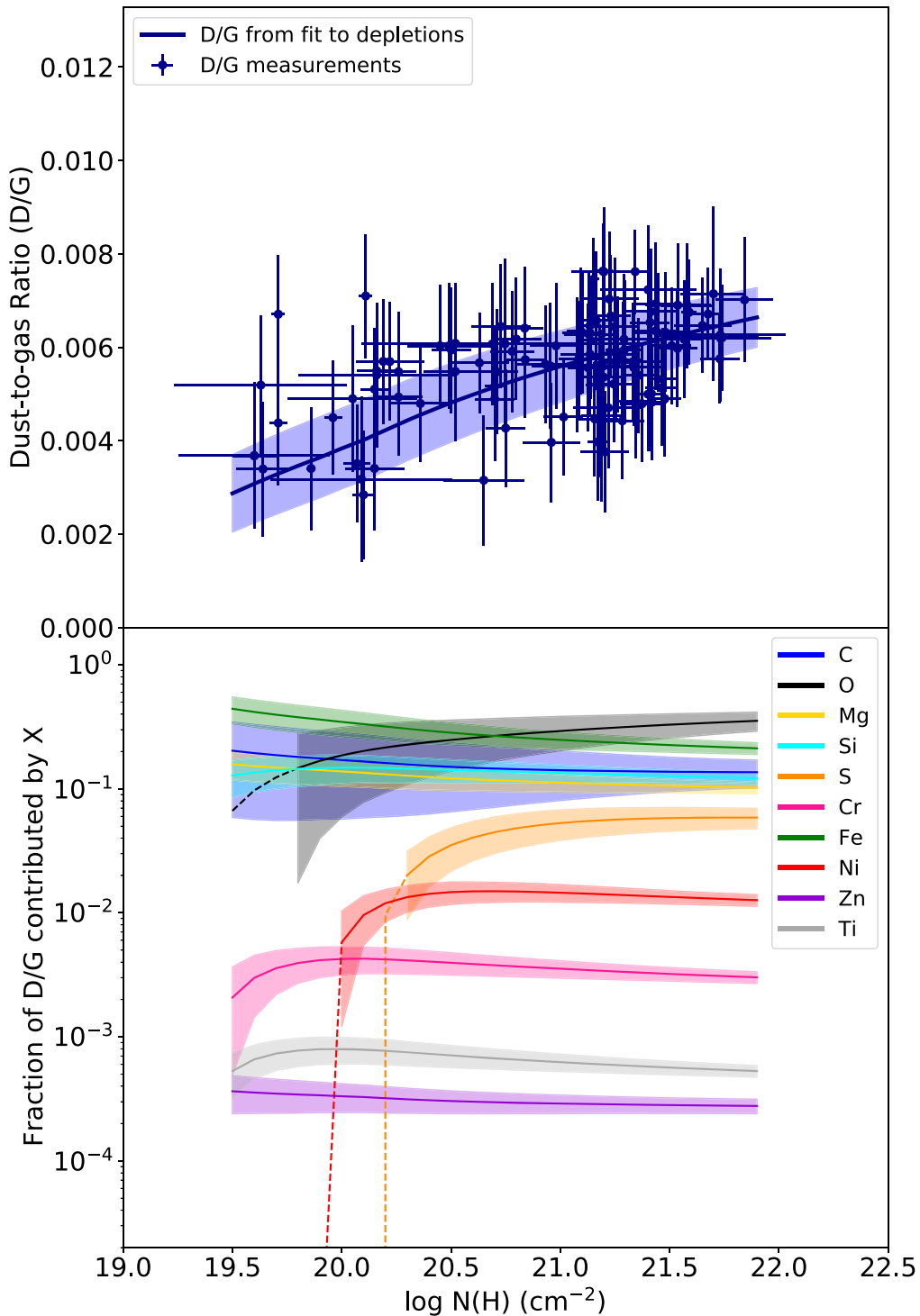


Figure 5. Top: dust-to-gas ratio (D/G) in the MW, obtained from the collection of depletions measured by Jenkins (2009), as a function of the logarithm of the hydrogen column density, $N(\text{H})$ (blue points and band). The points are measurements for each sight line, while the blue line and band were obtained from the fits of the individual depletions with $\log N(\text{H})$ and their 1σ uncertainty (coefficient of the fits are given in Table 3). Bottom: fraction of the dust mass contributed by each element, as a function of $\log N(\text{H})$. The fraction of D/G contributed by some elements (e.g., S) drops to zero at low column densities due to depletions crossing the theoretical maximum limit of zero.

We note that the total carbon abundance assumed in the MW to derive depletions impacts the dust composition estimated in the MW, LMC, and SMC (Figures 8 and 9). In this paper, we assumed the same carbon abundance as in the original study of MW depletions (Jenkins 2009, who take their abundances from Lodders 2003). If, instead, we assume the carbon abundance corresponding to the solar + GCE

model (matching our assumed O abundance for the MW) in Table 1 of Hensley & Draine (2021), or 331 ppm, the fraction of the dust mass contributed by carbon increases by 50%. In the MW at the lowest column densities, the fraction of the dust mass contributed by carbon increases from 20% to 30% upon the carbon abundance update. In the LMC and SMC, the dust mass fraction of carbon at the lowest column densities

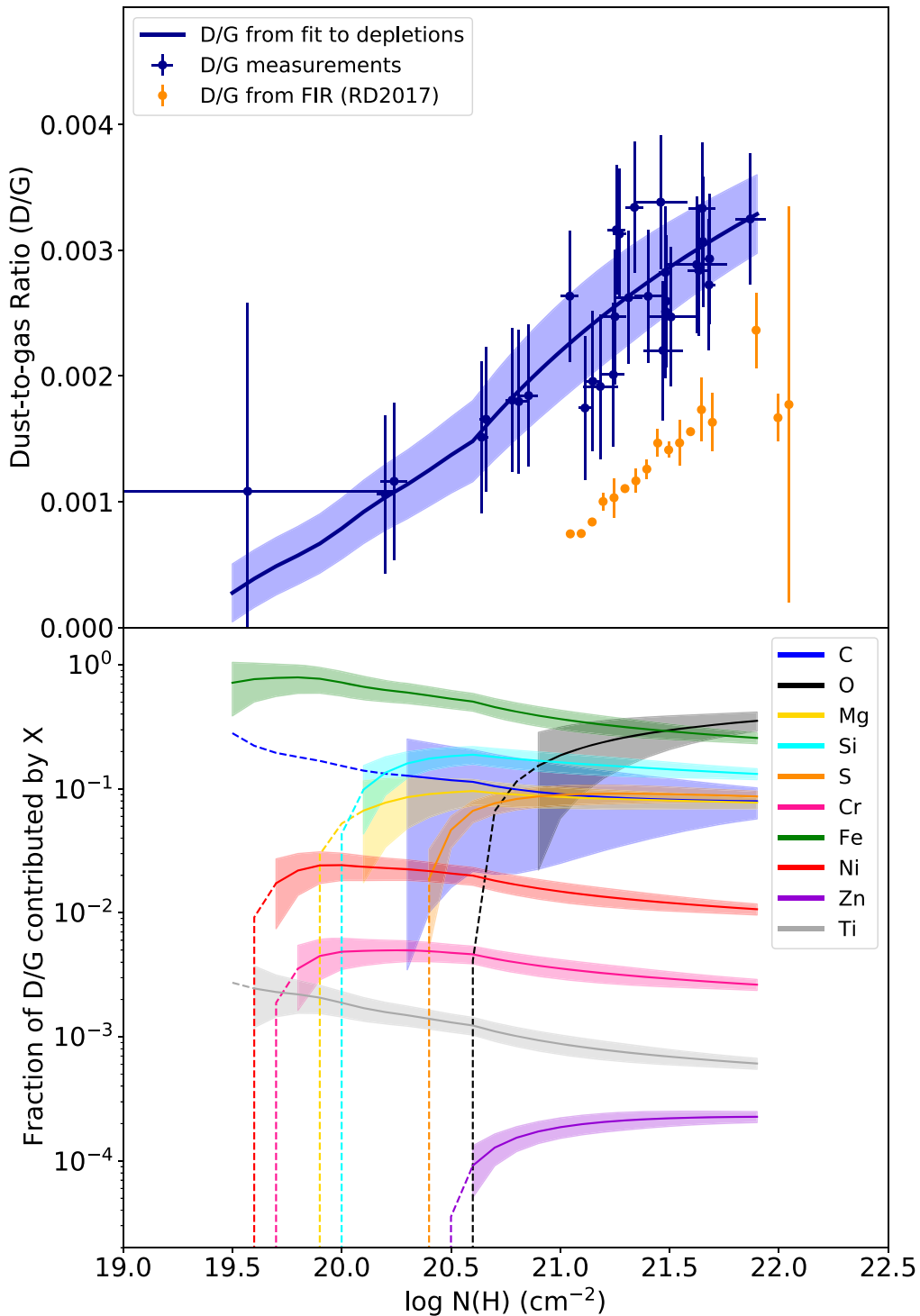


Figure 6. Top: dust-to-gas ratio (D/G) in the LMC, obtained from the collection of depletions measured by the METAL program (Roman-Duval et al. 2021), as a function of the logarithm of the hydrogen column density, $N(\text{H})$ (blue points and band). The points are measurements for each sight line, while the blue line and band were obtained from the fits of the individual depletions with $\log N(\text{H})$ and their 1σ uncertainty (coefficient of the fits are given in Table 3). For comparison, the D/G measured from FIR, 21 cm, and CO (1–0) emission in Roman-Duval et al. (2017) is shown in black. Bottom: fraction of the dust mass contributed by each element, as a function of $\log N(\text{H})$. The fraction of D/G contributed by some elements (e.g., S) drops to zero at low column densities due to depletions crossing the theoretical maximum limit of zero.

increases to 45% (instead of 30%) and 75% (instead of 55%), respectively.

7. Depletions, D/M, and D/G versus Metallicity

Chemical evolution models, such as Asano et al. (2013) or Feldmann (2015) predict that metallicity is an important factor

in setting the abundance of dust in galaxies (in addition to density, as seen in Section 5). Fundamentally, this is expected because the timescale for dust growth in the ISM is inversely proportional to metallicity (see, e.g., Equation (20) in Asano et al. 2013). With large samples of depletions in the MW, LMC ($Z = 0.5 Z_{\odot}$), and SMC ($Z = 0.2 Z_{\odot}$), we can put constraints on

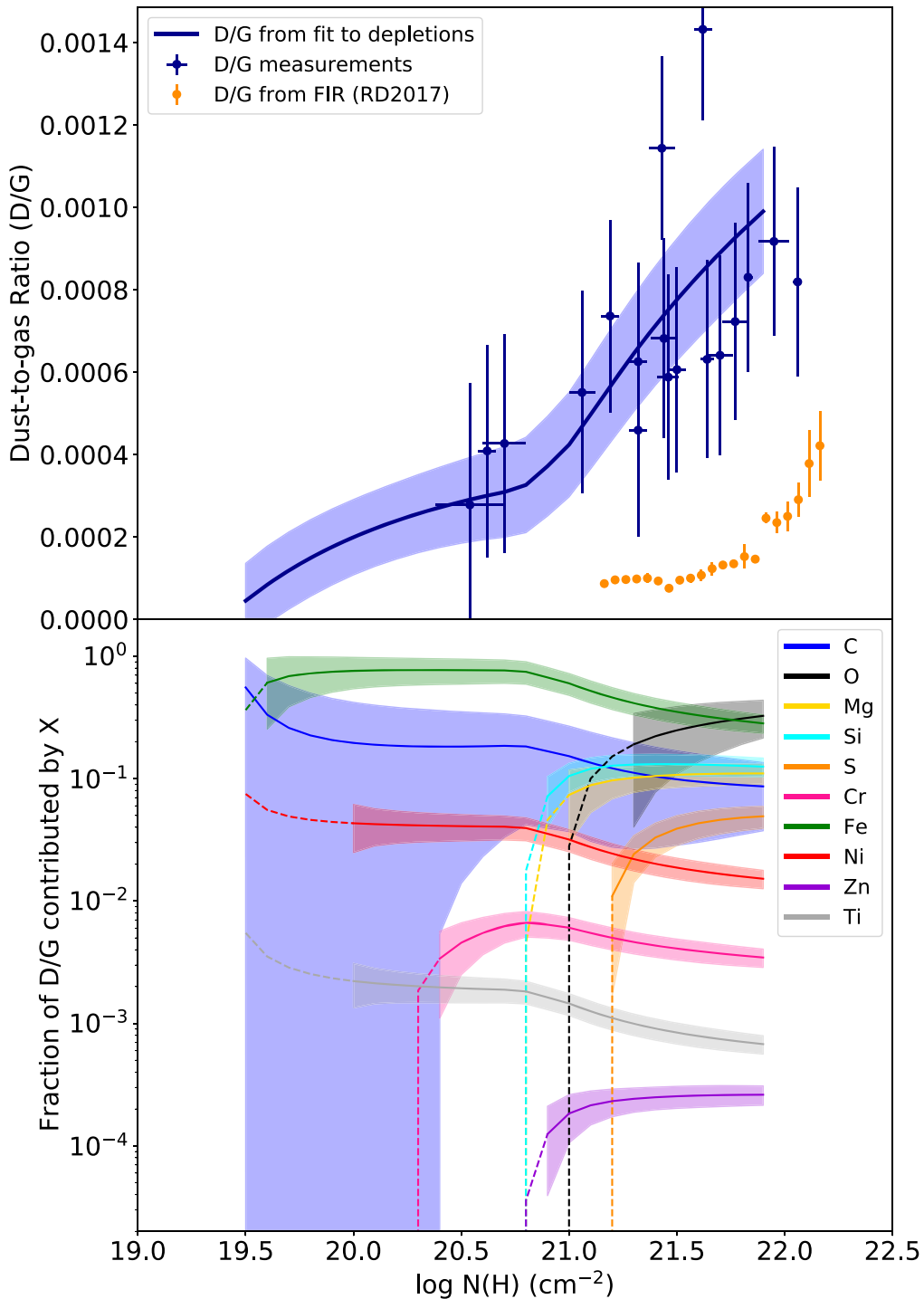


Figure 7. Top: dust-to-gas ratio (D/G) in the SMC, obtained from the collection of depletions measured by Jenkins & Wallerstein (2017), as a function of the logarithm of the hydrogen column density, $N(\text{H})$ (blue points and band). The points are measurements for each sight line, while the blue line and band were obtained from the fits of the individual depletions with $\log N(\text{H})$ and their 1σ uncertainty (coefficient of the fits are given in Table 3). For comparison, the D/G measured from FIR, 21 cm, and CO 1–0 in Roman-Duval et al. (2017) is shown in black. Bottom: fraction of the dust mass contributed by each element, as a function of $\log N(\text{H})$. The fraction of D/G contributed by some elements (e.g., S) drops to zero at low column densities due to depletions crossing the theoretical maximum limit of zero.

the variations of depletions, D/M , and D/G with metallicity down to 20% solar metallicity.

7.1. Depletions and D/M versus Metallicity

Despite the relatively small differences in the slopes of the $\log N(\text{H})-\delta(X)$ relation between the MW, LMC, and SMC seen in Figure 4, a clear trend with metallicity emerges: for all

elements, the relation between $\log N(\text{H})$ and $\delta(X)$ lies lowest for the MW (most depleted) and highest for the SMC (least depleted), with the LMC between those two extremes. This trend was already observed in Roman-Duval et al. (2019), based on Si only. Taking the mean depletion difference between the MW and LMC or SMC from Table 4 for all elements we can measure in all three galaxies (Mg, Si, S, Cr,

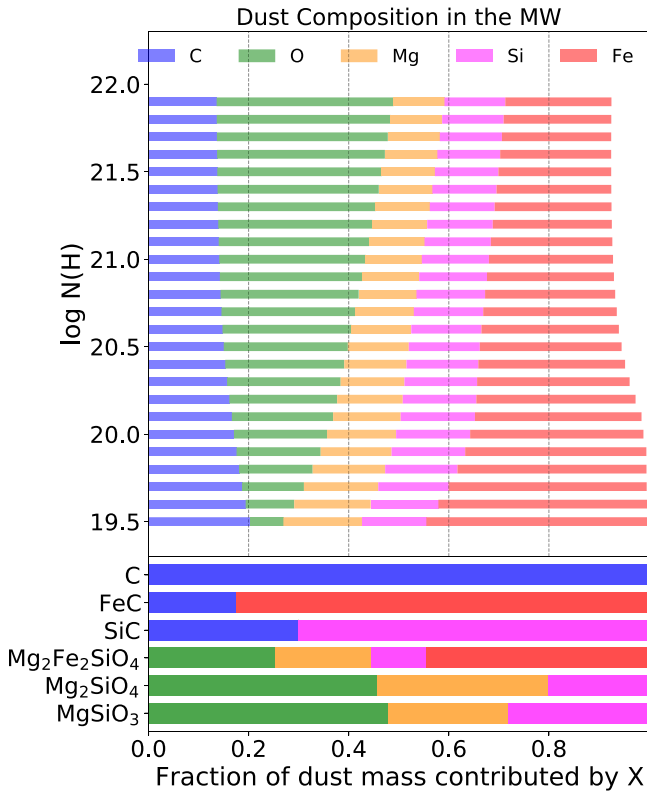


Figure 8. Top: dust composition (i.e., fraction of the dust mass contributed by each element, C, O, Mg, Si, and Fe) as a function of $\log N(\text{H})$ in the MW. At high column densities, the fractions of the dust mass from C, O, Mg, Si, and Fe do not add up to one due to the contribution from other elements (S and Ni) not plotted here. Bottom: mass fractions of C, O, Mg, Si, and Fe for known condensates: C (graphite), FeC (iron carbide), SiC (silicon carbide), and silicates (olivine ($\text{Mg}_2\text{Fe}_2\text{SiO}_4$), forsterite (Mg_2SiO_4), enstatite (MgSiO_3)).

Fe, Ni, Zn, and Ti), and weighting the mean depletion difference by the inverse square of the errors, we obtain mean weighted depletion differences of 0.46 ± 0.01 between the MW and LMC, and 0.80 ± 0.02 dex between the MW and SMC, at $\log N(\text{H}) = 21 \text{ cm}^{-2}$. This implies that the fraction of metals other than C and O in the gas is 2.9 times higher in the LMC than in the MW, and 6.3 times higher in the SMC than the MW.

Because the fraction of metals locked in dust, given by $1 - 10^{-\delta(X)}$, remains fairly high, even at the metallicity of the SMC, the differences in D/M between the three galaxies are much less pronounced than the differences in gas-phase fractions, given by $10^{\delta(X)}$. This is shown in Figure 10, where we plot the fraction of elements in dust and the D/M as a function of metallicity (using the depletion values in Table 4) for $\log N(\text{H}) = 21 \text{ cm}^{-2}$. For example, the fraction of Fe in the gas phase is about five times higher in the SMC than in the MW (0.67 dex difference in depletion at $\log N(\text{H}) = 21 \text{ cm}^{-2}$; see Table 4), but the fraction of Fe in the dust phase only subsequently decreases from 97% (MW) to 88% (SMC). The fractions of C and O in the dust are relatively low, which could in principle lead to larger variations in dust-phase fractions between the MW, LMC, and SMC. However, the differences in gas-phase C and O fractions between the MW, LMC, and SMC are not very large. The reason for this small difference is that the slopes A_C and A_O of depletions versus F_* in the MW are very shallow (-0.101 and -0.22 , respectively). Thus, even if the depletions of Fe (and all other elements except C and O) in

the LMC and SMC are 0.4 dex and 0.7 dex less negative than in the MW, corresponding to F_* being lower by -0.25 and -0.5 , respectively, the corresponding difference in C depletions is only 10% of the difference in F_* , hence 0.03 dex between the MW and LMC, and 0.05 dex between the MW and the SMC. Similarly, the difference in O depletions is 22% of the difference in F_* , or 0.06 dex between the MW and LMC, and 0.11 dex between the MW and SMC. As a result, the D/M in the LMC is only 25% lower than in the MW at $\log N(\text{H}) = 21 \text{ cm}^{-2}$. In the SMC, the D/M is a factor of three lower than in the MW at $\log N(\text{H}) = 21 \text{ cm}^{-2}$.

7.2. Impact of the Varying D/M on Neutral Gas-phase Metallicities in the MW, LMC, and SMC

The trends of depletions and D/M with metallicity observed in Section 7.1 have a surprising result on the neutral gas-phase metallicities of the MW, LMC, and SMC. Because the total metallicity of the MW is five times higher than that of the SMC, but the fraction of metals (other than C and O) in the gas in the MW is six times lower than in the SMC, the neutral gas-phase metallicities of these two galaxies should be about the same for a given hydrogen column density. Similarly, the total metallicity of the LMC is two times lower than that of the MW, but the fraction of metals in the gas in the LMC is 2.5 times higher than in the MW, and so the neutral gas-phase metallicities of the MW and LMC should be similar at a fixed hydrogen column density. Figure 11 confirms that, for a given $\log N(\text{H})$, the neutral gas-phase metallicities of the MW, LMC, and SMC are about the same, despite the masses of these galaxies differing by two orders of magnitude: $M_*(\text{MW}) \sim 6 \times 10^{10} M_\odot$ (Licquia & Newman 2015), $M_*(\text{LMC}) = 2.7 \times 10^9 M_\odot$ (van der Marel 2006, pp. 47–71), and $M_*(\text{SMC}) = 3.1 \times 10^8 M_\odot$ (Besla 2015).

A direct consequence of this effect is that, without further information on the depletion levels from abundance ratios (e.g., De Cia et al. 2016, 2018), DLA systems with metallicities similar to the MW and Magellanic Clouds at high redshift would be indistinguishable based on their gas-phase metallicities measured from QSO spectroscopy. This is particularly important given that volatile elements such as S and Zn, used as metallicity tracers in such systems, do deplete from the gas phase. Recovering the total metallicity of volatile elements in DLAs therefore requires accurate depletion corrections. Such corrections have been derived using abundance ratios in DLAs ($[\text{Zn}/\text{Fe}]$) and the MW calibration of the relation between $\delta(\text{Zn})$ and $[\text{Zn}/\text{Fe}]$ (De Cia et al. 2016). This effect provides additional motivation for deriving calibrations of the $[\text{Zn}/\text{Fe}]$ -depletion relation in the MW, LMC, and SMC, and testing them on DLAs, which will be presented in the upcoming METAL IV paper (J. Roman-Duval et al. 2022, in preparation).

7.3. D/G versus Metallicity from Depletions

We estimate the D/G in each galaxy (MW, LMC, and SMC) for a given $\log N(\text{H})$ using the approach described in Section 5.2, by basically summing the mass-weighted dust fractions of the elements for which we measure depletions, as well as C and O for which we estimate depletions using the method outlined in Section 3.3 (see also Table 4 for numerical values of depletions used in the calculation of D/G). The resulting D/G values for $\log N(\text{H}) = 20, 21, \text{ and } 22 \text{ cm}^{-2}$ are listed in Table 5. The D/G in the MW, LMC, and SMC is

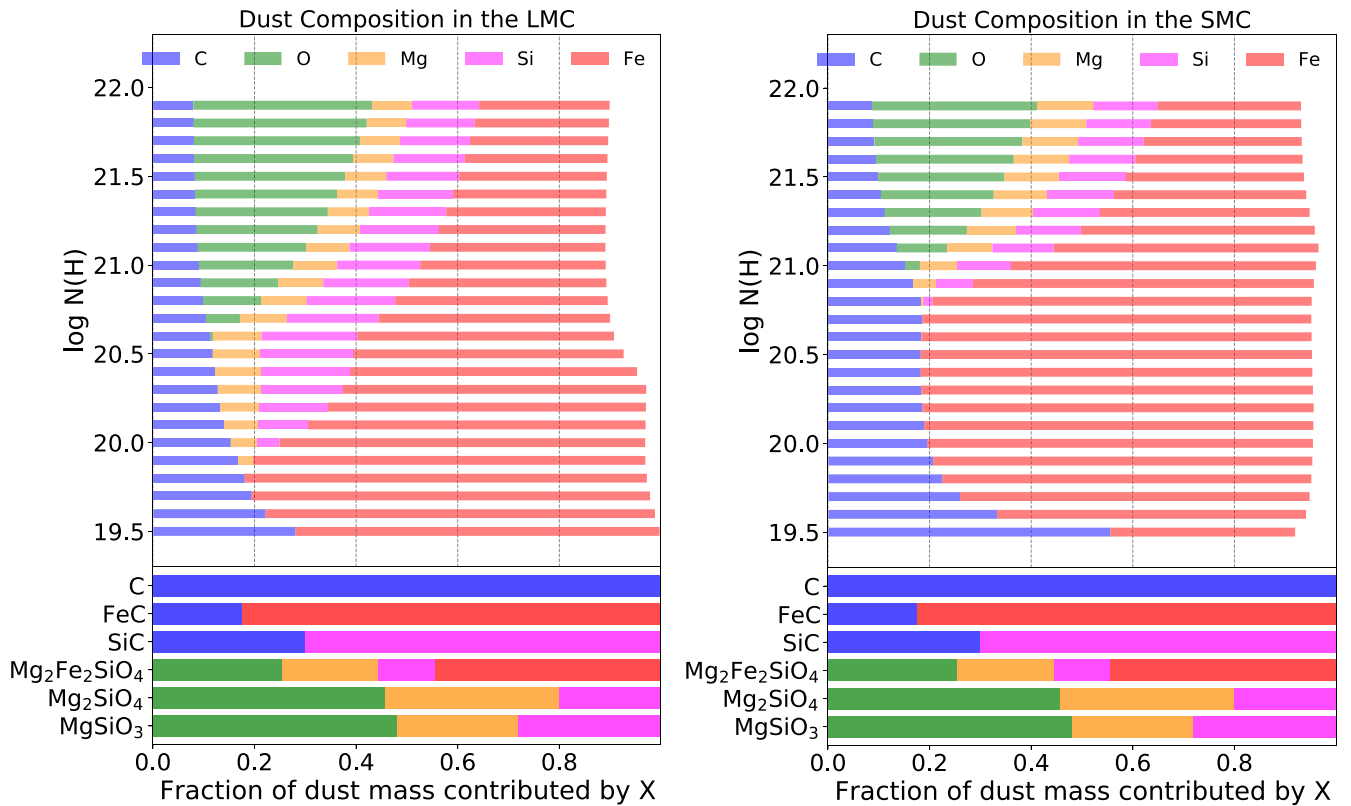


Figure 9. Same as Figure 8, but for the LMC (left) and SMC (right).

plotted in Figure 12 for $\log N(\text{H}) = 21 \text{ cm}^{-2}$. At $\log N(\text{H}) = 21 \text{ cm}^{-2}$, the D/G in the LMC is a factor of 2.6 lower than in the MW, while the SMC D/G is 13 times smaller than in the MW. The latter value of D/G in the SMC is in excellent agreement with result of Yanchulova Merica-Jones et al. (2021), who found from extinction modeling that $\langle A_V/N_H \rangle$ in the SMC is 14 times smaller than in the MW.

This decrease of D/G with metallicity is steeper than linear, as expected from a D/M that also decreases with metallicity. Indeed, we showed in Section 7.1 that the SMC D/M is a factor 2–3 lower than in the MW. The variation of D/G with metallicity inferred from depletion measurements in the MW, LMC, and SMC are consistent with the chemical evolution model from Feldmann (2015) (plotted in Figure 12) that takes into account dust formation in evolved stars, dust growth in the ISM, dust destruction by SNe shocks, and dust dilution by inflows of pristine gas. The model is plotted for a plausible range of the parameter γ , which is the ratio of the molecular gas consumption by star formation timescale (typically 2 Gyr; see Bigiel et al. 2008) to the timescale for dust growth in the ISM in the MW (typically 10 Myr; see Hirashita 2000; Asano et al. 2013; Feldmann 2015). In Figure 12, γ ranges from 2×10^3 to 10^6 with a fiducial value $\gamma = 3 \times 10^4$. In the model, above a critical metallicity at which the dust input rate from evolved stars (AGB + supernovae) and ISM dust growth balances the dust destruction by SN shockwaves and dilution by inflows of pristine gas, the D/M is high, with most metals locked in the dust phase. Below this critical metallicity, the D/M is low and determined by the input of stellar dust sources. The metallicity of the SMC (20% solar) still lies above the critical metallicity where the D/M and therefore D/G starts to decrease steeply with metallicity. Depletion measurements at metallicities 10% solar or lower are needed to fill this gap in our understanding of

the dust abundance and chemical evolution of galaxies. This is the subject of an ongoing investigation using data taken as part of the HST large program METAL-Z (G0-15880; A. Hamanowicz et al. 2022, in preparation).

7.4. D/G versus Metallicity: Comparison with FIR Measurements

The D/G estimates in the MW, LMC, and SMC derived from depletion measurements complement previous FIR measurements of D/G versus metallicity (Rémy-Ruyer et al. 2014; Roman-Duval et al. 2017; De Vis et al. 2019) in nearby galaxies, including the LMC and SMC. The FIR-based dust masses (or surface densities for resolved galaxies) are estimated by modeling the FIR SED observed with facilities such as Herschel, Spitzer, or Planck with either modified blackbodies (e.g., Gordon et al. 2014; Roman-Duval et al. 2017, in the LMC and SMC) or full dust models (e.g., Galliano et al. 2011; Rémy-Ruyer et al. 2014, 2015; Chasten et al. 2017; De Vis et al. 2019; Aniano et al. 2020; Chasten et al. 2021). The atomic and molecular gas masses (or gas surface density) are estimated from HI 21 cm and CO rotational emission. The LMC and SMC are highly resolved, and therefore the D/G can be measured as a function of $\log N(\text{H})$ as in Roman-Duval et al. (2017), or in an integrated manner (total dust mass/total gas mass).

The D/G obtained from depletions corresponds to pencil beam sight lines of a given $\log N(\text{H})$, from which we can infer the trend of D/G versus $\log N(\text{H})$ via linear fits, as done in Section 5.2. However, D/G measurements obtained from the FIR in nearby galaxies are integrated and correspond to the ratio of the total dust mass to the total gas mass. To estimate an integrated D/G from depletions and be able to compare it to

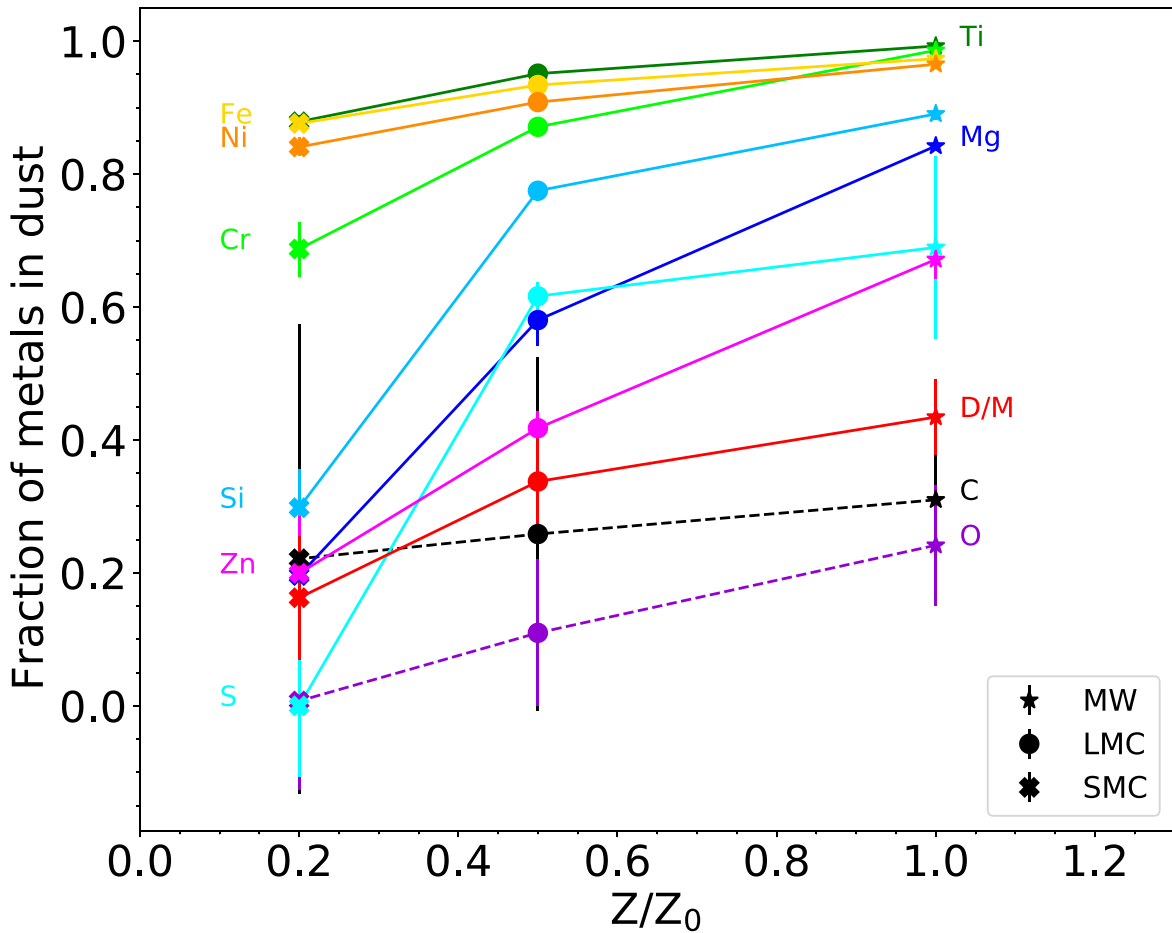


Figure 10. Fraction of elements C, O, Mg, Si, S, Cr, Fe, Ni, Zn, and Ti in the dust as a function of metallicity based on measurements the MW, LMC, and SMC at $\log N(\text{H}) = 21 \text{ cm}^{-2}$. The D/M, obtained from the mass-weighted sum of abundances of elements in the dust, is also plotted (also for $\log N(\text{H}) = 21 \text{ cm}^{-2}$).

integrated FIR-based measurements, we apply the relation between D/G and $\log N(\text{H})$ established from depletions shown in Figures 5, 6, and 7, $(D/G)_{\text{dep}}$, to the $\log N(\text{H})$ distribution observed with 21 cm emission ($N(\text{H})_{21\text{cm}}$) in the maps from Stanimirovic et al. (1999) for the SMC and Kim et al. (2003) for the LMC:

$$(D/G)_{\text{int}} = \frac{\sum_{\text{pix}} N(\text{H})_{21\text{cm}} (D/G)_{\text{dep}} (N(\text{H})_{21\text{cm}})}{\sum_{\text{pix}} N(\text{H})_{21\text{cm}}}. \quad (13)$$

The different D/G estimates in the MW, LMC, SMC (FIR and depletions) and nearby galaxies (FIR only) are shown in Figure 12 as a function of (total) metallicity. For the LMC and SMC, we plot the integrated D/G. The chemical evolution model from Feldmann (2015) is also shown. A few key points stand out in Figure 12.

The first key conclusion from Figure 12 is that the FIR-based and depletion-based D/G in the LMC and SMC differ by factors of two and five, respectively, reflecting the differences previously observed in the relation between D/G and $\log N(\text{H})$. Roman-Duval et al. (2021) discussed possible reasons for this observed discrepancy. First, because the FIR surface brightness observed by Herschel, Spitzer, and Planck is the product of the dust surface density and dust opacity, an estimate of the dust surface density is degenerate with the assumed opacity, which can vary and is not well-constrained observationally or theoretically (Stepnik et al. 2003; Köhler et al. 2012; Roman-Duval et al. 2014; Demyk et al. 2017). As a result, the

FIR-based dust mass estimates suffer from systematic uncertainties of a factor of a few, even when the dust temperature can be accurately constrained using multiband photometry. Observational constraints on the dust FIR opacity obtained by comparing the FIR emission observed in Herschel to extinction maps obtained from HST imaging at a range of metallicities are needed to resolve this discrepancy. This problem is the focus of several HST imaging programs in the LMC and SMC (Scylla, a parallel program to ULLYSES; PI: Claire Murray); METAL GO-14675 (Roman-Duval et al. 2019); SMIDGE (Yanchulova Merica-Jones et al. 2017, 2021), in IC 1613 at 15% solar metallicity and Sextans A at 8% solar metallicity (GO-16513; PI: Roman-Duval), and in Leo-P at 3% solar metallicity (GO-16222; PI: Christopher Clark). We note that, in estimating dust masses from the FIR, there is also a potential bias (underestimation of the dust mass) due to the integrated nature of the measurement of dust surface densities that can vary on small scales (Galliano et al. 2011).

Gas masses estimated from 21 cm and CO emission are not immune from such substantial systematics either. The molecular gas mass estimates rely on an assumed CO-to-H₂ conversion factor (Bolatto et al. 2013), which is also poorly constrained and degenerate with D/G measurements (Roman-Duval et al. 2014). Another potential issue in estimating atomic gas masses from 21 cm emission is that masses are often estimated from integrated measurements associated with a region that is spatially more extended than the region detected

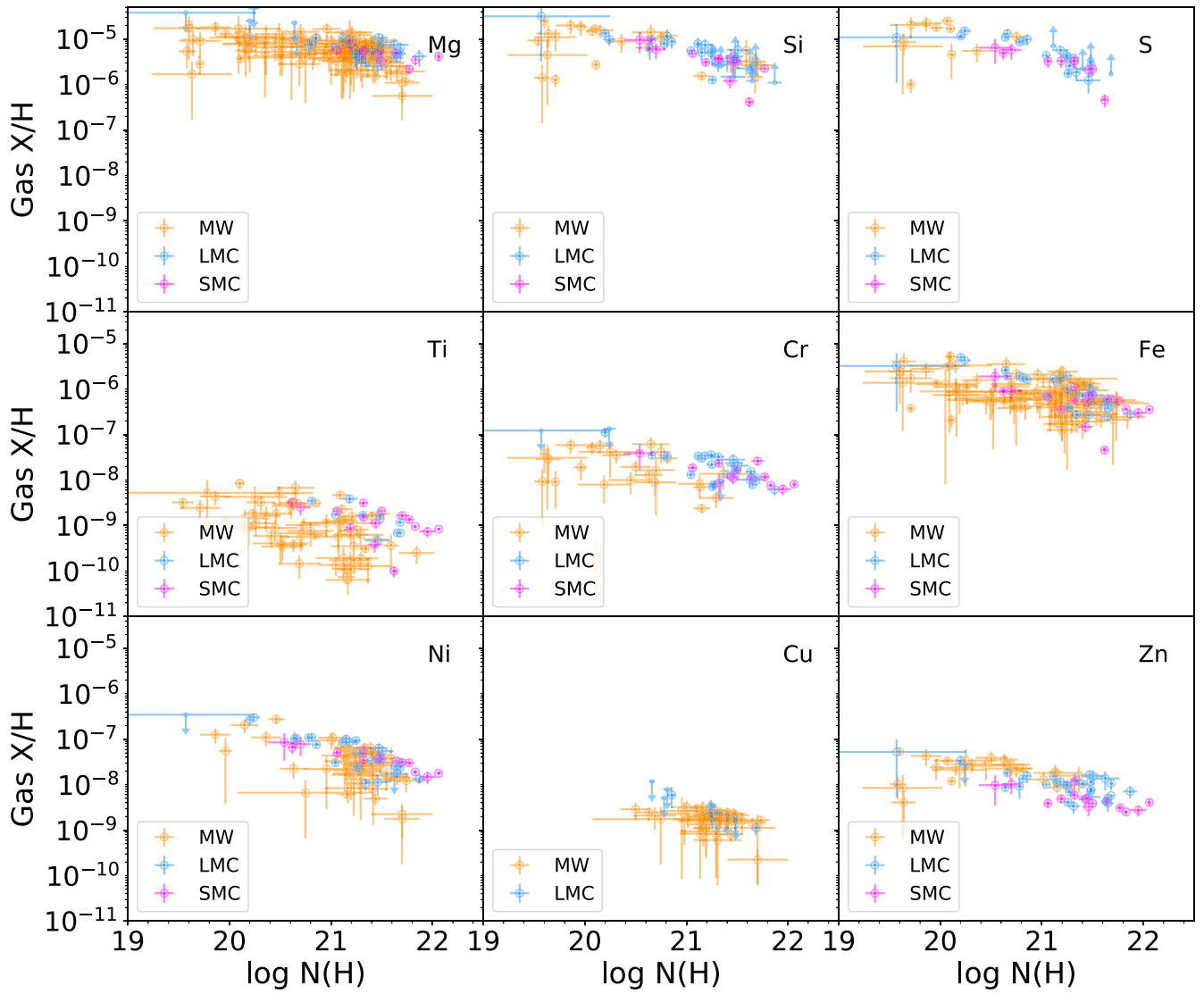


Figure 11. Gas-phase abundances of Mg, Si, S, Cr, Fe, Ni, Cu, Zn, Ti, and Cr, as a function of $\log N(\text{H})$. Orange, blue, and magenta correspond to the Milky Way (Jenkins 2009), LMC (Roman-Duval et al. 2021), and SMC (Jenkins & Wallerstein 2017), respectively. For a given hydrogen column density, the gas-phase abundances in the MW, LMC, and SMC are similar, despite the total metallicities of these galaxies differing by respective factors of two and five. This is due to the lower fraction of metals locked into dust grains at low metallicity.

Table 5
D/G Values Obtained from Depletions and FIR in the MW, LMC, and SMC

	MW	LMC		SMC	
	Depletions	Depletions	FIR ^a	Depletions	FIR ^a
D/G $\log N(\text{H}) = 20 \text{ cm}^{-2}$	$(3.83 \pm 1.03) \times 10^{-3}$	$(7.87 \pm 7.6) \times 10^{-4}$	$(7.43 \pm 0.58) \times 10^{-4}$	$(1.99 \pm 3.51) \times 10^{-4}$	$(8.68 \pm 1.91) \times 10^{-5}$
D/G $\log N(\text{H}) = 21 \text{ cm}^{-2}$	$(5.59 \pm 0.74) \times 10^{-3}$	$(2.19 \pm 0.49) \times 10^{-3}$	$(8.38 \pm 0.66) \times 10^{-4}$	$(4.24 \pm 2.56) \times 10^{-4}$	$(8.68 \pm 1.91) \times 10^{-5}$
D/G $\log N(\text{H}) = 22 \text{ cm}^{-2}$	$(6.74 \pm 0.57) \times 10^{-3}$	$(3.38 \pm 0.30) \times 10^{-3}$	$(1.77 \pm 3.15) \times 10^{-3}$	$(1.03 \pm 0.16) \times 10^{-3}$	$(3.78 \pm 1.60) \times 10^{-4}$
D/G Integrated	$(5.98 \pm 0.65) \times 10^{-3}$	$(2.30 \pm 0.11) \times 10^{-3}$	$(1.27 \pm 0.12) \times 10^{-3}$	$(7.57 \pm 0.8) \times 10^{-4}$	$(1.56 \pm 0.17) \times 10^{-4}$

Note.

^a The FIR D/G values are from Roman-Duval et al. (2017).

in dust emission (either on the sky or along the line of sight), leading to a possible overestimation of the gas mass. Thus, the systematic uncertainty on D/G estimates based on emission tracers could very well amount to a factor of several, perhaps up to an order of magnitude, and the effects describe above would preferentially underestimate the D/G.

On the depletions' side, the main source of systematic uncertainty is the poorly constrained contribution of C and O to the D/G estimated from depletions. Indeed, the estimates of C and O depletions rely on the MW relation between depletions of different elements, which might not apply at low metallicity, due to different abundance ratios and subsequent chemical affinities.

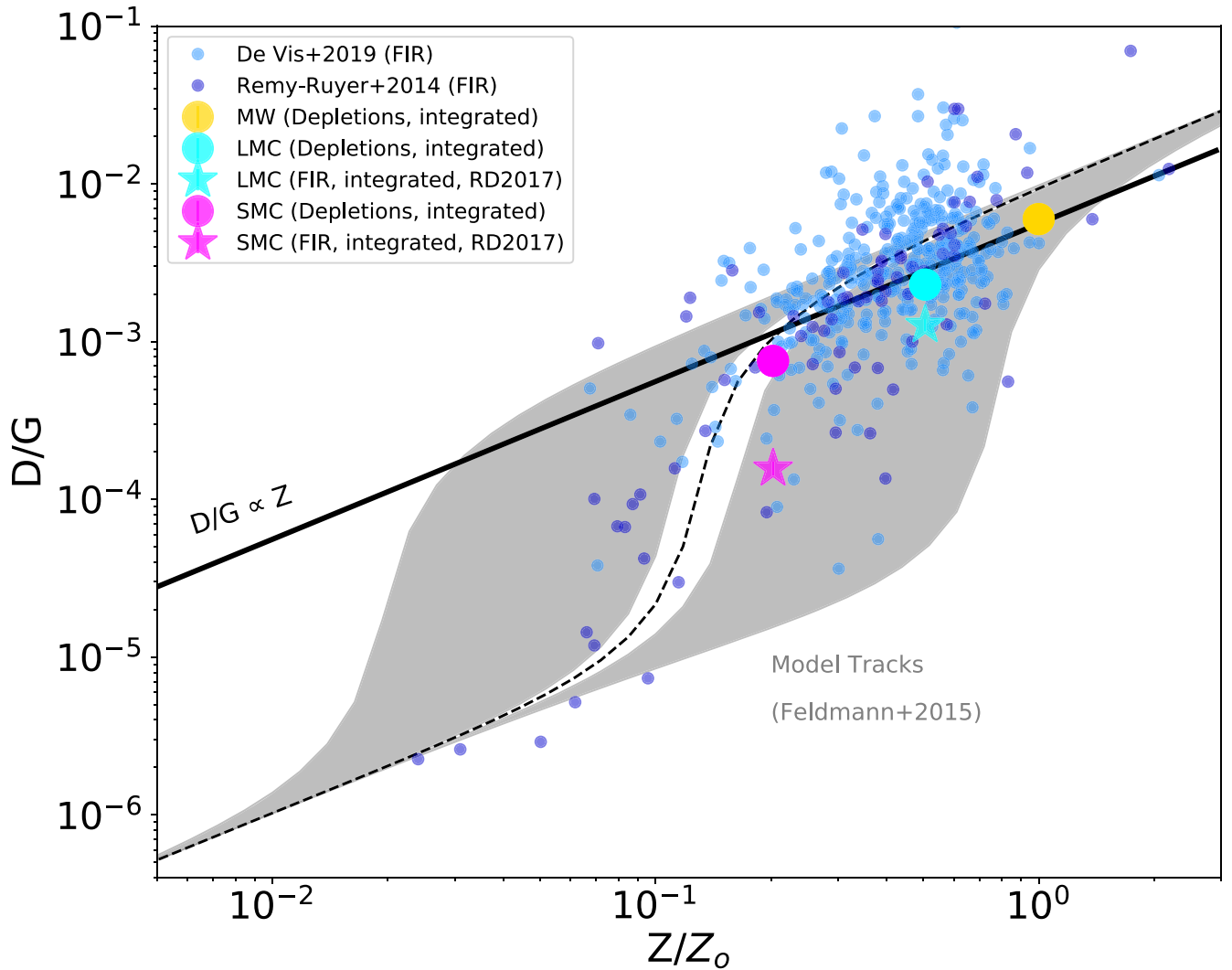


Figure 12. Dust-to-gas ratio as a function of total (gas + dust) metallicity in different systems and from different observational methods. The blue points correspond to the D/G measured in nearby galaxies using FIR emission to trace dust, and 21 cm and CO rotational emission to trace atomic and molecular gas (Rémy-Ruyer et al. 2014; De Vis et al. 2019). The cyan and magenta stars correspond to similar measurements in the LMC and SMC, respectively (Roman-Duval et al. 2017). The FIR measurements are integrated (total dust mass/total gas mass). The yellow, cyan, and magenta circles show D/G measurements obtained from spectroscopic depletions in the MW, LMC, and SMC (Jenkins 2009; Jenkins & Wallerstein 2017; Roman-Duval et al. 2021). The D/G estimated from depletions is integrated using the approach described in Section 7.4. Finally, the gray tracks show the chemical evolution model from Feldmann (2015) for a range of the γ parameter ($2 \times 10^3 - 10^6$).

Additionally, the trend of C depletions versus F_* in the MW were only measured toward a few sight lines and are therefore highly uncertain (as shown by the error on the fits shown in Figure 5 of Jenkins 2009). Therefore, it is possible that the depletion levels of C and O (and D/G) may be over- or underestimated. We will have to wait until a LUVOIR-like observatory with enough UV sensitivity to observe the weak C and O lines outside the MW and observationally constrain the depletions of C and O at low metallicity. In the meantime, the uncertain contribution of C and O to the dust mass budget should be captured in our error bars (which explains why there are more likely fits to the trend of D/G versus $\log N(\text{H})$ at higher D/G values than the fiducial relation in Figures 5, 6, and 7).

A last source of discrepancy between the FIR and depletion-based D/G presented in Roman-Duval et al. (2021) is the different geometrical setups of depletion and FIR observations can lead to different outcomes in the trend of D/G versus $\log N(\text{H})$, as demonstrated based on simulations in Roman-Duval et al. (2021).

8. Conclusion

We compiled and compared gas-phase abundance and depletion measurements in the Milky Way, LMC (50% solar metallicity), and SMC (20% solar metallicity).

The relation between the depletion of Fe and that of other elements is relatively invariant between the MW, LMC, and SMC, with the only exceptions being Mg and Ti showing 3σ – 4σ differences between the MW, LMC, and SMC. Correspondingly, the relation between difference abundance ratios of refractory to volatile elements follow the same invariance between the three galaxies examined here. This implies that the depletion of Fe, which is easy to measure thanks to the numerous UV transitions of this element with a wide range of oscillator strengths, combined with the calibration of the $\delta(\text{Fe})$ – $\delta(\text{X})$ relation established in the Milky Way and Magellanic Clouds, can be used to estimate the depletion of elements in systems (such as more distant galaxies) where depletions for elements other than Fe are difficult to observe spectroscopically. Such

calibrations will be derived in the next METAL paper (METAL IV).

In the MW, LMC, and SMC, the depletions of all elements observed become more negative (i.e., less metals in the gas phase, more metals in the dust phase) as the column density of hydrogen increases. Over the column density range $\log N(\text{H}) = 20\text{--}22 \text{ cm}^{-2}$, the fraction of metals in the gas phase typically decreases by 0.3 dex (Zn) to 1.3 dex (e.g., Fe, Ni, Cr, S, and Si), but can decrease by as much as 2 dex (for Ti and Cr in the MW). As a result, the dust-to-gas ratio D/G increases by a factor of 3–4 from $\log N(\text{H}) = 20$ to 22 cm^{-2} in all three galaxies. This is consistent with the shorter timescales for accretion of gas-phase metals onto dust grains as the density of the ISM increases.

By comparing the depletions in the MW, LMC, and SMC, we establish that the fraction of metals in the gas phase increases with decreasing metallicity. The difference in the fraction of metals in the gas phase amounts to a factor of three between the MW and LMC, and a factor of six between the MW and the SMC. Correspondingly, the fraction of metals locked in dust (the dust-to-metal ratio, D/M) decreases with decreasing metallicity. The D/M is a factor of 1.2 lower in the LMC compared to the MW, and a factor of 2–3 lower in the SMC than the MW. The immediate, albeit surprising, consequence of this variable D/M is that the neutral gas-phase metallicities of the MW, LMC, and SMC, for a given hydrogen column density, are very similar, despite the total metallicities of the LMC and SMC being lower than the MW's by respective factors of two and five. Indeed, in the SMC (resp. LMC), the total abundance of metals is five (resp. two) times lower than in the MW, but six (resp. three) times less metals are locked away in dust grains, leaving the gas-phase abundances about the same as in the MW.

By summing the depletions over the elements for which depletions are measured, as well as C and O, for which we estimate depletions based on the MW relation between Fe and C or O depletions, we obtain D/G values of $(5.59 \pm 0.74) \times 10^{-3}$, $(2.19 \pm 0.49) \times 10^{-3}$, and $(4.24 \pm 2.56) \times 10^{-4}$ for the MW, LMC, and SMC at $\log N(\text{H}) = 21 \text{ cm}^{-2}$. Integrating over the H I distribution observed via 21 cm emission, the D/G for the MW, LMC, and SMC are $(5.98 \pm 0.65) \times 10^{-3}$, $(2.30 \pm 0.11) \times 10^{-3}$ and $(7.57 \pm 0.80) \times 10^{-4}$, respectively.







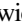





We infer the dust composition in each galaxy from the depletions, and find that, while iron, carbon, and silicate components (Mg, Si, and O) contribute equally to the dust budget in the MW, this is not the case in the LMC and SMC, where iron and carbon dominate the dust mass budget at all but the highest column densities ($\log N(\text{H}) > 22 \text{ cm}^{-2}$).

Since $D/G \propto D/M \times Z$ and D/M decreases with decreasing metallicity, the D/G observed through depletions decreases nonlinearly (steeper than linearly) with metallicity. This is consistent with the predictions from chemical evolution models that include dust formation, growth, destruction, and dilution processes (e.g., Feldmann 2015). This result is also consistent with the D/G–Z relation observed in nearby galaxies using the FIR to trace dust, 21 cm emission to trace atomic gas, and CO rotational emission to measure the mass of molecular gas (Rémy-Ruyer et al. 2014; De Vis et al. 2019). However, the depletion-based D/G is a factor of a few (two for the LMC, five for the SMC) higher than the D/G derived from FIR, 21 cm, and CO rotational emission. A combination of the uncertain dust FIR opacity, geometric effects, and the uncertainty of the

depletion-based D/G due to the lack of C and O depletion measurements outside the MW, could explain this discrepancy. Nevertheless, both measurements are in agreement with chemical evolution models, owing to the metallicities of the LMC and SMC being higher than or on the cusp of the critical metallicity at which the D/M and D/G sharply drop. Below this critical metallicity of 10%–20% solar, the D/G predicted by chemical evolution models and observed in the FIR drops abruptly with metallicity. The models would interpret this finding as the growth of dust in the ISM becoming too inefficient below a critical metallicity of 10%–20% solar to counteract the effects of dust destruction in SN shocks and dust dilution from pristine inflows. No depletion measurements are yet available at those metallicities, but they will soon be available from the METAL-Z large HST program (GO-15880, A. Hamanowicz et al. 2022, in preparation).

We thank the referee for providing insightful comments and suggestions. Edward B. Jenkins, Benjamin Williams, Karl Gordon, Karin Sandstrom, and Petia Yanchulova Merica-Jones acknowledge support from grant No. HST-GO-14675. This work is based on observations with the NASA/ESA Hubble Space Telescope obtained at the Space Telescope Science Institute, which is operated by the Associations of Universities for Research in Astronomy, Incorporated, under NASA contract NAS5-26555. These observations are associated with program 14675. Support for Program number 14675 was provided by NASA through a grant from the Space Telescope Science Institute, which is operated by the Association of Universities for Research in Astronomy, Incorporated, under NASA contract NAS5-26555.

ORCID iDs

Julia Roman-Duval  <https://orcid.org/0000-0001-6326-7069>
 Edward B. Jenkins  <https://orcid.org/0000-0003-1892-4423>
 Kirill Tchernyshyov  <https://orcid.org/0000-0003-0789-9939>
 Christopher J. R. Clark  <https://orcid.org/0000-0001-7959-4902>
 Annalisa De Cia  <https://orcid.org/0000-0003-2082-1626>
 Karl D. Gordon  <https://orcid.org/0000-0001-5340-6774>
 Aleksandra Hamanowicz  <https://orcid.org/0000-0002-4646-7509>
 Vianney Lebouteiller  <https://orcid.org/0000-0002-7716-6223>
 Marc Rafelski  <https://orcid.org/0000-0002-9946-4731>
 Karin Sandstrom  <https://orcid.org/0000-0002-4378-8534>
 Jessica Werk  <https://orcid.org/0000-0002-0355-0134>
 Petia Yanchulova Merica-Jones  <https://orcid.org/0000-0002-9912-6046>

References

- Aniano, G., Draine, B. T., Hunt, L. K., et al. 2020, *ApJ*, 889, 150
 Asano, R. S., Takeuchi, T. T., Hirashita, H., & Inoue, A. K. 2013, *EP&S*, 65, 213
 Asplund, M., Grevesse, N., Sauval, A. J., & Scott, P. 2009, *ARA&A*, 47, 481
 Besla, G. 2015, arXiv:1511.03346
 Bigiel, F., Leroy, A., Walter, F., et al. 2008, *AJ*, 136, 2846
 Bolatto, A. D., Leroy, A. K., Jameson, K., et al. 2011, *ApJ*, 741, 12
 Bolatto, A. D., Wolfire, M., & Leroy, A. K. 2013, *ARA&A*, 51, 207
 Chasteney, J., Bot, C., Gordon, K. D., et al. 2017, *A&A*, 601, A55
 Chasteney, J., Sandstrom, K., Chiang, I.-D., et al. 2019, *ApJ*, 876, 62
 Chasteney, J., Sandstrom, K., Chiang, I. D., et al. 2021, *ApJ*, 912, 103
 Chiang, I. D., Sandstrom, K. M., Chasteney, J., et al. 2018, *ApJ*, 865, 117
 Chiang, I.-D., Sandstrom, K. M., Chasteney, J., et al. 2021, *ApJ*, 907, 29
 Clark, C. J. R., De Vis, P., Baes, M., et al. 2019, *MNRAS*, 489, 5256
 da Silveira, C. R., Barbuy, B., Friaça, A. C. S., et al. 2018, *A&A*, 614, A149

- De Cia, A. 2018, *A&A*, 613, L2
- De Cia, A., Ledoux, C., Mattsson, L., et al. 2016, *A&A*, 596, A97
- De Cia, A., Ledoux, C., Petitjean, P., & Savaglio, S. 2018, *A&A*, 611, A76
- De Vis, P., Jones, A., Viana, S., et al. 2019, *A&A*, 623, A5
- Delgado Mena, E., Moya, A., Adibekyan, V., et al. 2019, *A&A*, 624, A78
- Demyk, K., Meny, C., Leroux, H., et al. 2017, *A&A*, 606, A50
- Duffau, S., Caffau, E., Sbordone, L., et al. 2017, *A&A*, 604, A128
- Ernandes, H., Barbuy, B., Alves-Brito, A., et al. 2018, *A&A*, 616, A18
- Feldmann, R. 2015, *MNRAS*, 449, 3274
- Galliano, F., Galametz, M., & Jones, A. P. 2018, *ARA&A*, 56, 673
- Galliano, F., Hony, S., Bernard, J.-P., et al. 2011, *A&A*, 536, A88
- Gordon, K. D., Roman-Duval, J., Bot, C., et al. 2014, *ApJ*, 797, 85
- Hensley, B. S., & Draine, B. T. 2021, *ApJ*, 906, 73
- Herrera-Camus, R., Fisher, D. B., Bolatto, A. D., et al. 2012, *ApJ*, 752, 112
- Hill, V., Andrievsky, S., & Spite, M. 1995, *A&A*, 293, 347
- Hirashita, H. 2000, *PASJ*, 52, 585
- Jenkins, E. B. 2009, *ApJ*, 700, 1299
- Jenkins, E. B., & Wallerstein, G. 2017, *ApJ*, 838, 85
- Kim, S., Staveley-Smith, L., Dopita, M. A., et al. 2003, *ApJS*, 148, 473
- Kisielius, R., Kulkarni, V. P., Ferland, G. J., et al. 2015, *ApJ*, 804, 76
- Köhler, M., Stepnik, B., Jones, A. P., et al. 2012, *A&A*, 548, A61
- Licquia, T. C., & Newman, J. A. 2015, *ApJ*, 806, 96
- Lodders, K. 2003, *M&PSA*, 38, 5272
- Lodders, K. 2021, *SSRv*, 217, 44
- Mattsson, L. 2020, *MNRAS*, 491, 4334
- Morton, D. C. 2003, *ApJS*, 149, 205
- Oppenheimer, B. D., & Davé, R. 2008, *MNRAS*, 387, 577
- Péroux, C., & Howk, J. C. 2020, *ARA&A*, 58, 363
- Quiret, S., Péroux, C., Zafar, T., et al. 2016, *MNRAS*, 458, 4074
- Rafelski, M., Wolfe, A. M., Prochaska, J. X., Neeleman, M., & Mendez, A. J. 2012, *ApJ*, 755, 89
- Rémy-Ruyer, A., Madden, S. C., Galliano, F., et al. 2014, *A&A*, 563, A31
- Rémy-Ruyer, A., Madden, S. C., Galliano, F., et al. 2015, *A&A*, 582, A121
- Roman-Duval, J., Bot, C., Chastenot, J., & Gordon, K. 2017, *ApJ*, 841, 72
- Roman-Duval, J., Gordon, K. D., Meixner, M., et al. 2014, *ApJ*, 797, 86
- Roman-Duval, J., Jenkins, E. B., Tchernyshyov, K., et al. 2021, *ApJ*, 910, 95
- Roman-Duval, J., Jenkins, E. B., Williams, B., et al. 2019, *ApJ*, 871, 151
- Rowlands, K., Gomez, H. L., Dunne, L., et al. 2014, *MNRAS*, 441, 1040
- Russell, S. C., & Dopita, M. A. 1992, *ApJ*, 384, 508
- Schruba, A., Leroy, A. K., Walter, F., et al. 2011, *AJ*, 142, 37
- Stanimirovic, S., Staveley-Smith, L., Dickey, J. M., Sault, R. J., & Snowden, S. L. 1999, *MNRAS*, 302, 417
- Stepnik, B., Abergel, A., Bernard, J.-P., et al. 2003, *A&A*, 398, 551
- Tchernyshyov, K., Meixner, M., Seale, J., et al. 2015, *ApJ*, 811, 78
- van der Marel, R. P. 2006, in *The Local Group as an Astrophysical Laboratory*, ed. M. Livio & T. M. Brown, Vol. 17 (Cambridge: Cambridge Univ. Press)
- Welty, D. E., & Crowther, P. A. 2010, *MNRAS*, 404, 1321
- Yanchulova Merica-Jones, P., Sandstrom, K. M., Johnson, L. C., et al. 2017, *ApJ*, 847, 102
- Yanchulova Merica-Jones, P., Sandstrom, K. M., Johnson, L. C., et al. 2021, *ApJ*, 907, 50
- Zhukovska, S., Dobbs, C., Jenkins, E. B., & Klessen, R. S. 2016, *ApJ*, 831, 147